

## ChronoFlow: A Data-Driven Model for Gyrochronology

PHIL R. VAN-LANE,<sup>1,2</sup> JOSHUA S. SPEAGLE (沈佳士),<sup>3,1,2,4</sup> GWENDOLYN M. EADIE,<sup>3,1,4</sup> STEPHANIE T. DOUGLAS,<sup>5</sup>  
PHILLIP A. CARGILE,<sup>6</sup> CATHERINE ZUCKER,<sup>6</sup> YUXI (LUCY) LU,<sup>7,8</sup> AND RUTH ANGUS<sup>9,10</sup>

<sup>1</sup>*David A. Dunlap Department of Astronomy & Astrophysics, University of Toronto, Toronto, ON, Canada*

<sup>2</sup>*Dunlap Institute of Astronomy & Astrophysics, University of Toronto, Toronto, ON, Canada*

<sup>3</sup>*Department of Statistical Sciences, University of Toronto, Toronto, ON M5S 3G3, Canada*

<sup>4</sup>*Data Sciences Institute, University of Toronto, Toronto, ON, Canada*

<sup>5</sup>*Department of Physics, Lafayette College, Easton, PA, United States*

<sup>6</sup>*Center for Astrophysics — Harvard & Smithsonian, Cambridge, MA 02138, USA*

<sup>7</sup>*Department of Astronomy, The Ohio State University, Columbus, 140 W 18th Ave, OH 43210, USA*

<sup>8</sup>*Center for Cosmology and Astroparticle Physics (CCAPP), The Ohio State University, 191 W. Woodruff Ave., Columbus, OH 43210, USA*

<sup>9</sup>*American Museum of Natural History, Central Park West, Manhattan, NY, USA*

<sup>10</sup>*Center for Computational Astrophysics, Flatiron Institute, Manhattan, NY, USA*

### ABSTRACT

Gyrochronology is a technique for constraining stellar ages using rotation periods, which change over a star’s main sequence lifetime due to magnetic braking. This technique shows promise for main sequence FGKM stars, where other methods are imprecise. However, models have historically struggled to capture the observed rotational dispersion in stellar populations. To properly understand this complexity, we have assembled the largest standardized data catalog of rotators in open clusters to date, consisting of  $\approx 7,400$  stars across 30 open clusters/associations spanning ages of 1.5 Myr to 4 Gyr. We have also developed **ChronoFlow**: a flexible data-driven model which accurately captures observed rotational dispersion. We show that **ChronoFlow** can be used to accurately forward model rotational evolution, and to infer both cluster and individual stellar ages. We recover cluster ages with a statistical uncertainty of 0.06 dex ( $\approx 15\%$ ), and individual stellar ages with a statistical uncertainty of 0.7 dex. Additionally, we conducted robust systematic tests to analyze the impact of extinction models, cluster membership, and calibration ages on our model’s performance. These contribute an additional 0.06 dex of uncertainty in cluster age estimates, resulting in a total error budget of 0.08 dex. We estimate ages for the NGC 6709 open cluster and the Theia 456 stellar stream, and calculate revised rotational ages for M34, NGC 2516, NGC 1750, and NGC 1647. Our results show that **ChronoFlow** can precisely estimate the ages of coeval stellar populations, and constrain ages for individual stars. Furthermore, its predictions may be used to inform physical spin down models. **ChronoFlow** will be publicly available at <https://github.com/philvanlane/chronoflow>.

### 1. INTRODUCTION

Stellar ages are critically important to astronomy on a wide range of scales, from exoplanet evolution models to galactic archaeology (e.g., Soderblom 2010). Since its introduction by Demarque & Larson (1964), isochrone fitting has been the most ubiquitous technique for dating stars of a known coeval population. This is done by comparing the observed photometry for stars of various masses against theoretical stellar evolution models, e.g. on a color-magnitude diagram (CMD). However, since stars evolve very little on a CMD over their main sequence (MS) lifetimes, isochrone fitting is imprecise

without stars on the giant branch that can be used to locate the MS turn off.

Asteroseismology (e.g., Cunha et al. 2007; Silva Aguirre et al. 2017) has become another popular stellar dating technique, which uses pulsations caused by pressure and gravity waves within stars to infer their internal composition and therefore evolutionary stage. However, pulsations are difficult to detect in low mass MS stars, since the signal magnitude is directly related to the size of the star.

Lithium depletion, which occurs via nuclear reactions in stellar cores, offers yet another way to estimate ages. Lower-mass stars deplete lithium slower because they are cooler, so the Lithium Depletion Boundary (LDB;

i.e. the lowest mass stars that have fully consumed their lithium) serves as an age indicator for stellar populations. Analyzing the LDB (e.g., Jeffries 2014; Beck et al. 2017; Deliyannis et al. 2019) has worked well for stars and clusters ( $\lesssim 200$  Myr), but requires spectroscopy to measure Lithium equivalent widths ( $EW_{Li}$ ), and is not well constrained at older ages due to the flattening of Lithium depletion. As an example, Jeffries et al. (2023b) used an empirical model to estimate individual stellar ages and cluster ages up to 6 Gyr. They achieved precisions of 0.1 dex in the best-constrained cases (M dwarfs  $\lesssim 100$  Myr), but noted that their recovery of training ages struggled at  $\gtrsim 1$  Gyr.

A stellar dating technique that has proven useful for low mass MS stars is gyrochronology. Gyrochronology is applicable to any stars with a convective envelope ( $\sim$  late F and GKM classes, including fully convective M dwarfs), because these stars lose angular momentum over time due to the ejection of material via magnetized winds. This angular momentum loss is observable as a decrease in rotation rate. This theory of “magnetic braking” was first proposed by Schatzman (1962), and refined further by e.g., Kraft (1967), Wilson (1966), and Weber & Davis (1967). Skumanich (1972) proposed the first quantitative empirical model describing this stellar spin down:  $P_{rot} \propto \tau^{\frac{1}{2}}$  (where  $P_{rot}$  is the rotation period and  $\tau$  is the age of a star).

Gyrochronology took another step forward with foundational papers by Barnes (2003, 2007), who proposed a new empirical model featuring “fast” and “slow” evolutionary tracks. In these models, stellar spin down only depended on color (B-V). Barnes (2010) and Barnes & Kim (2010) developed this further into spindown models which are dependent on the Rossby number  $R_o$  (the ratio of rotation period to convective turnover time) of a star.

Recently, space-based missions such as *Kepler* (Borucki et al. 2010), *K2* (Howell et al. 2014) and the *Transiting Exoplanet Survey Satellite* (*TESS*; Ricker et al. 2015) have yielded abundant time series photometry and subsequently rotation period measurements. This has enabled a wealth of gyrochronology research, from the enhancement of theoretical spindown models (e.g., van Saders et al. 2016; Spada & Lanzafame 2020; Gossage et al. 2021) to the development of data-driven empirical models (e.g., Angus et al. 2015, 2019; Curtis et al. 2019; Boyle & Bouma 2022).

One important consideration is the age calibration required to build empirical models. Historically, isochrone fitting to open clusters has been the predominant method (e.g., Godoy-Rivera et al. 2021; Long et al. 2023), which has become increasingly reliable with

the precise photometry produced by *Gaia* DR2 (van Leeuwen et al. 2018) and beyond. Some studies have also applied asteroseismology (e.g., Angus et al. 2015; van Saders et al. 2016; Hall et al. 2021) and wide binaries (e.g., Pass et al. 2022; Silva-Beyer et al. 2022; Chiti et al. 2024) as age calibration mechanisms.

Across all of these physical and empirical studies, however, many nuances of the stellar rotational evolution evade simple analytical models. These include:

1. Weakened magnetic braking and change in rotational evolution of field age stars (Angus et al. 2015; van Saders et al. 2016; Hall et al. 2021; Metcalfe et al. 2022; Silva-Beyer et al. 2022).
2. Distinct differences in spindown behaviour between partially convective and fully convective M dwarfs (Chiti et al. 2024; Lu et al. 2024b).
3. Separation of fully convective M dwarfs into fast and slow rotators (Garraffo et al. 2018; Pass et al. 2022).
4. Observational scatter in the  $P_{rot}$ - $\tau$ -mass space has not been well constrained by physical or empirical models to date (e.g., Curtis et al. 2019, 2020; Bouma et al. 2023; Lu et al. 2024a).

These challenges necessitate a completely flexible, data-driven model that can properly capture these observational trends.

To achieve this flexibility, we previously presented the first machine learning (ML) based gyrochronology model proof of concept (Van-Lane et al. 2023), and two other recent studies have also probed the flexibility of empirical models. Bouma et al. (2023) developed an interpolation framework which fits the fast and slow rotator sequences to two normal distributions. Lu et al. (2024a) implemented a Gaussian Process calibrated against seven open clusters and gyro-kinematic ages for  $\approx 46,000$  field stars. While these methods capture some of the dispersion seen in observations, they still require constraints on the models’ functional form.

In this work we present our updated model: **ChronoFlow**, which *does not impose any constraints on the functional form of rotational evolution*, and accurately captures observational scatter. We have expanded on our data catalog from Van-Lane et al. (2023) by: (i) including literature rotation periods for 30 open clusters and associations; (ii) standardizing to Gaia DR3 photometry; and (iii) de-reddening using 3D dustmaps from Edenhofer et al. (2023) and Green et al. (2019). We have also optimized our training architecture and

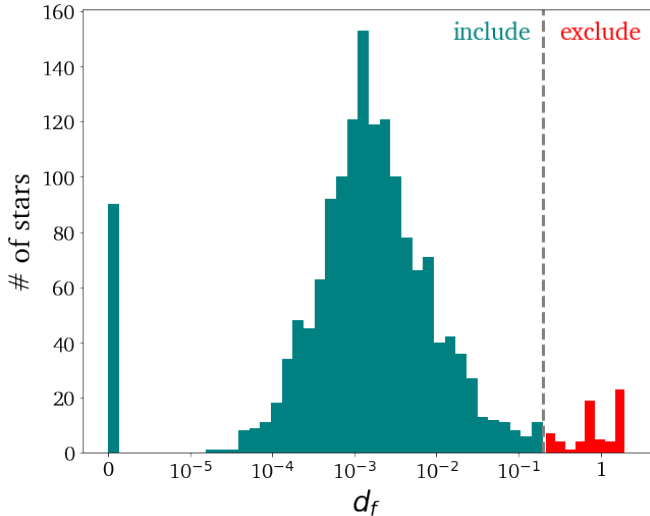


**Figure 1.** Distribution of the fractional difference ( $d_f$ ) in  $P_{rot}$  for stars having two measurements. The value we use as a quality cut (0.2) is illustrated by the dashed grey line. The value of 0.2 was chosen to exclude the tail of stars with very discrepant  $P_{rot}$  measurements, while keeping the large majority of these stars.

enhanced the model itself, which now incorporates photometric uncertainties and cluster membership probabilities.

The rest of the paper is structured as follows. §2 outlines how we have assembled our final catalog, cross-matched all rotation periods to Gaia DR3 (Gaia Collaboration et al. 2023), applied photometric uncertainties, and assigned cluster membership probabilities to all stars. §3 describes the statistical framework for our model, and §4 details the model itself. §5 presents our results, including age recovery tests. In §6 we describe all of the systematic uncertainties that we have characterized, and quantify our model’s performance. We outline applications for ChronoFlow in §7, including new age estimates for five clusters and one stellar stream, and we conclude in §8.

## 2. CATALOG OF OPEN CLUSTER ROTATORS

We conducted a literature search for stellar rotation periods in 30 open clusters and associations, and our compiled catalog is presented in Table 1. It includes four key types of data; we outline these briefly here and describe them further in §2.1-2.4.

1. *Rotation periods.* We compiled rotation periods ( $P_{rot}$ ) from 15 literature catalogs. Many of these are themselves compilations, so we trace all rotation periods back to their original measurements. Details are discussed in §2.1.

2. *Photometry.* Where Gaia DR3 IDs were not provided in the source catalog, we crossmatched the stars to DR3 using right ascension (R.A.) and declination (Decl.), and compared magnitudes from the source catalog to DR3 where the crossmatch based on R.A. and Decl. was ambiguous. We de-reddened the DR3 photometry using both the Edenhofer et al. (2023) and Green et al. (2019) dustmaps, and propagated the parallax and extinction errors to our de-reddened colors. These details are discussed in §2.2.

3. *Cluster membership probability.* We assigned a quantitative cluster membership probability to each star. Our primary source for this was HDB-Scan (McInnes et al. 2017), with which the probabilities were computed as described in §2.1 of Douglas et al. (2024). We reverted to the membership probabilities from the source catalogs where HDB-Scan probabilities were not available. Details are discussed in §2.3.

4. *Cluster ages.* We conducted a literature review of age estimates for the clusters in our catalog; these are compiled in Table 2 and Figure 4.

### 2.1. Rotation periods

We started with 15,723 rotation periods compiled from all sources in Table 1. After trimming this list based on quality cuts recommended in the source papers and single-star criteria from each data catalog, 11,427 rotation periods remained. The details of these cuts are described in Appendix B. Since many of our clusters are in multiple data catalogs, there were two types of measurement duplication in these 11,427 periods:

1. Rotation period measurements cited in multiple data catalogs.
2. Multiple rotation period measurements for the same DR3 source.

To handle the first case, we identified the source of rotation measurement for all stars across the catalogs. In 420 cases, the same  $P_{rot}$  measurement was cited in multiple catalogs (see Appendix C), meaning that 11,007 out of our 11,427 rotation periods were *unique* measurements.

For the second case, we used the results of our Gaia DR3 crossmatch (see §2.2) to identify stars with rotation periods measured in multiple studies. We found that of the 11,007 measurements, there were 8,249 unique DR3 sources. Of these, 6,069 had a single  $P_{rot}$  measurement, 1,403 stars had two measurements, and 777 stars had three measurements. We include all of the stars with

a single  $P_{rot}$  in our catalog. For the stars with two  $P_{rot}$  measurements, we drop those having a fractional difference ( $d_f$ ) of  $\geq 20\%$  from our catalog (68 stars). Figure 1 visualizes this cut. While there was evidence that some of these might have been harmonics (where one  $P_{rot}$  is twice or half the value of the other), most did not appear to be. For stars having a fractional difference  $\geq 20\%$ , we took the average of the two as our  $P_{rot}$ .

For stars with three  $P_{rot}$  measurements, we first computed the fractional standard deviation of the three values. If it was  $\leq 2\%$ , we used the average. If not, we

compared the difference between the maximum value and middle value ( $d_{max}$ ) to the difference between the minimum value and the middle value ( $d_{min}$ ). If  $d_{max} > 3d_{min}$  or vice versa, we discarded the outlier. We then considered the fractional difference between the two remaining values. If this was  $\geq 20\%$ , we exclude the star from our catalog. If it was  $< 20\%$ , we used the average of the two as our  $P_{rot}$ . If  $d_{max}$  and  $d_{min}$  did not differ by more than  $3\times$  in either direction, we excluded the star if the fractional standard deviation of the three values was  $\geq 20\%$ , and used the average  $P_{rot}$  otherwise.

**Table 1.** Summary of  $P_{rot}$  sources. The *Data Catalog* is the literature source, the  *$P_{rot}$  Source* is the study in which the  $P_{rot}$  was measured, and the *Source Survey* is where the raw data came from. All individual  $P_{rot}$  records are provided in the machine-readable version of this table.

Cluster	Data Catalog	$P_{rot}$ Source	Source Survey	# of Rotators
$\alpha$ Persei	Boyle & Bouma (2022)	source catalog	TESS	238
Collinder 135	Douglas et al. (2024)	source catalog	TESS	204
H Persei	Moraux et al. (2013)	source catalog	CFHT, Maidanak, ZTSh, Byurakan	385
Hyades	Douglas et al. (2019)	source catalog	K2	54
		Delorme et al. (2011)	SuperWASP	18
		Douglas et al. (2016)	K2	23
		Hartman et al. (2011)	HATNet	2
		Kundert/Cargile (ASAS) <sup>1</sup>	ASAS	14
		Radick et al. (1987, 1995)	Lowell 0.5m	4
	Long et al. (2023)	source catalog	K2	88
		Delorme et al. (2011)	SuperWASP	9
	Hartman et al. (2011)	HATNet	1	
IC 2391	Douglas et al. (2024)	source catalog	TESS	96
IC 2602	Douglas et al. (2024)	source catalog	TESS	175
M34	Meibom et al. (2011)	source catalog	WIYN	68
M35	Long et al. (2023)	Libralato et al. (2016)	Kepler/K2	265
		Meibom et al. (2009)	WIYN	126
		Nardiello et al. (2015)	Schmidt Telescope	22
		Soares-Furtado et al. (2020)	K2	124
M37	Godoy-Rivera et al. (2021)	Hartman et al. (2009)	K2	340
M50	Godoy-Rivera et al. (2021)	Irwin et al. (2009)	Blanco telescope at CTIO	577
M67	Barnes et al. (2016)	source catalog	K2	17
	Dungee et al. (2022)	source catalog	CFHT	215
	Long et al. (2023)	source catalog	K2	62
	Dungee et al. (2022)	CFHT	45	
NGC 1647	Long et al. (2023)	source catalog	K2	35
NGC 1750	Long et al. (2023)	source catalog	K2	39
NGC 1758	Long et al. (2023)	source catalog	K2	21
NGC 1817	Long et al. (2023)	source catalog	K2	60
NGC 2281	Fritzewski et al. (2023)	source catalog	AIP STELLA I, IAC	116

Cluster	Data Catalog	$P_{rot}$ Source	Source Survey	# of Rotators
NGC 2451A	Douglas et al. (2024)	source catalog	TESS	129
NGC 2516	Godoy-Rivera et al. (2021)	Irwin et al. (2007)	Blanco telescope at CTIO	327
NGC 2547	Douglas et al. (2024)	source catalog	TESS	80
	Godoy-Rivera et al. (2021)	Irwin et al. (2008)	MPG/ESO	109
NGC 2548	Barnes et al. (2015)	source catalog	AIP STELLA I, IAC	59
NGC 3532	Fritzewski et al. (2021)	source catalog	Yale telescope at CTIO	228
NGC 6811	Curtis et al. (2020)	Curtis et al. (2019)	Kepler	163
	Godoy-Rivera et al. (2021)	Curtis et al. (2019)	Kepler	32
		unknown		3
		Santos et al. (2019)	Kepler	60
	Santos et al. (2021)	Kepler	118	
Long et al. (2023)	source catalog	Kepler	220	
NGC 6819	Curtis et al. (2020)	Meibom et al. (2015)	Kepler	28
	Long et al. (2023)	source catalog	Kepler	151
NGC 6866	Long et al. (2023)	source catalog	Kepler	124
NGC 752	Curtis et al. (2020)	Agüeros et al. (2018)	PTF	8
Pleiades	Curtis et al. (2020)	Rebull et al. (2016)	K2	304
	Godoy-Rivera et al. (2021)	Rebull et al. (2016)	K2	597
	Long et al. (2023)	source catalog	K2	552
Hartman et al. (2010)		HAT-9/HAT-10	104	
Praesepe	Godoy-Rivera et al. (2021)	Rebull et al. (2017)	K2	588
	Long et al. (2023)	source catalog	K2	692
		Delorme et al. (2011)	SuperWASP	30
Rampalli et al. (2021)	source catalog	K2	512	
$\rho$ Ophiucus	Long et al. (2023)	source catalog	K2	208
	Rebull et al. (2018)	source catalog	K2	72
Ruprecht 147	Curtis et al. (2020)	source catalog	K2;PTF	27
	Long et al. (2023)	source catalog	K2	34
		Curtis et al. (2020)	K2;PTF	7
Taurus	Long et al. (2023)	source catalog	K2	92
Upper Scorpius	Long et al. (2023)	source catalog	K2	583
	Rebull et al. (2018)	source catalog	K2	625
<b>Total</b>	<b>15 Data Catalogs</b>	<b>36 <math>P_{rot}</math> Sources</b>	<b>20 Source Surveys</b>	<b>11,427 Periods</b>

<sup>1</sup> These data were not published; see footnote 5 in §2.1 of Douglas et al. (2019).

With this process, only one star with three measured rotation periods was excluded from our catalog, and we were left with 8,181 stars with reliable rotation periods in total. We describe edge cases that we encountered when compiling these rotation periods in Appendix C.

## 2.2. Photometry

For consistency, we use Gaia DR3 BP and RP bands (Riello et al. 2021) for all photometry. Of the 11,427 compiled rotation periods, we could not find a DR3 crossmatch for 49 of them. Additionally, 170 of the stars that we did crossmatch belong in Taurus, Upper Scorpius, or  $\rho$  Ophiucus, but were not part of the Ratzenböck et al. (2023) or Krolkowski et al. (2021) catalogs (which

we use as our source of truth for those regions). We successfully crossmatched the other 11,208 rotators, using the steps described in Appendix D, corresponding to 8,181 unique DR3 sources. In our final training catalog we have excluded 21 sources that do not have both BP and RP photometry, and an additional 713 having Gaia RUWE values  $\geq 1.4$  (although these are included in the online table). This last criteria is intended to exclude likely binaries that made it through the source catalog cuts, although we recognize that there are caveats. This cut may not capture short-period binaries (e.g., El-Badry 2024; Grondin et al. 2024), and Penoyre et al. (2022) indicate that a cut of 1.25 is more appropriate for DR3. We include an outlier component in our model

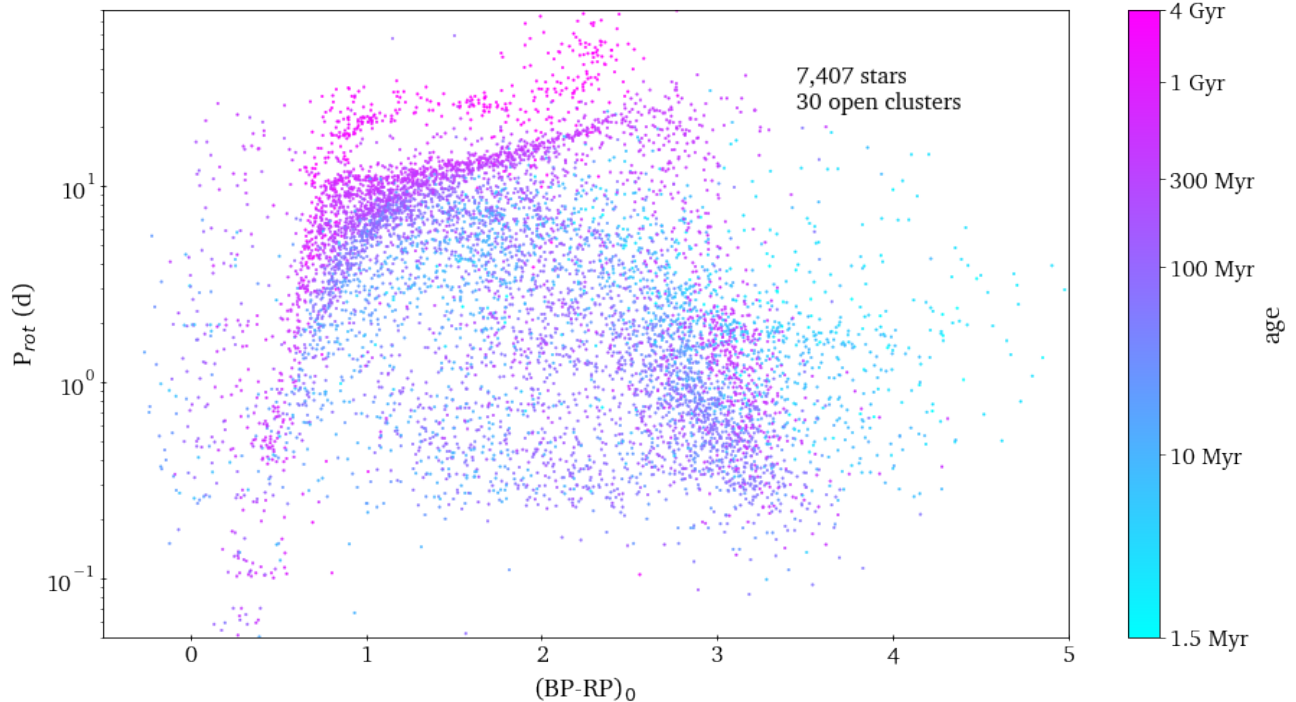


**Figure 2.** De-reddened color-rotation space for all stars in our final catalog. Stars are color-coded according to the age of their cluster. Older stars appear to have generally converged onto slowly rotating sequences more than younger stars.

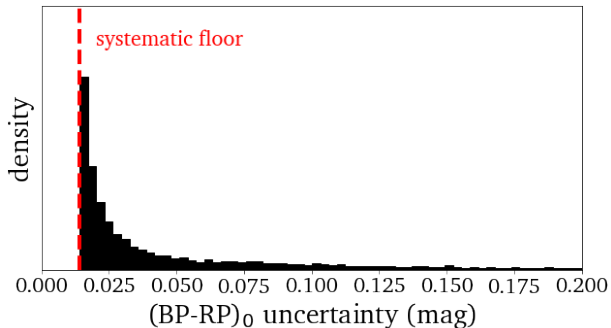


**Figure 3.** Distribution of  $(BP - RP)_0$  uncertainties. There is a minimum value of 0.01415 indicated by the red dashed line; this is the DR3 systematic floor corresponding to errors of 0.01 in the BP and RP bands. This plot is truncated at 0.2 mag, but there is a very thin tail that extends to 1.24 mag.

to account for binaries that remain in our sample, but acknowledge that handling this more thoughtfully in the future could help our model performance (see §4).

Finally, we apply a cut to exclude non-MS stars. While many of the source catalogs have already been vetted for these, we have performed a final CMD check, and excluded an additional 37 stars (see Appendix A). After these cuts, our final catalog consists of 7,407 unique Gaia DR3 MS sources with reliable rotation periods. These are plotted in Figure 2.

### 2.2.1. Stellar de-reddening

The effect of foreground dust needs to be accounted for. Since dust absorbs and scatters more light at short wavelengths (e.g., Cardelli et al. 1989), this *extinction* affects the BP band more than the RP band, and therefore influences  $(BP - RP)$ . We correct for this by de-reddening every star based on 3D dust maps.

For every star within 1.25 kpc, we used the Edenhofer et al. (2023) map because it provides parsec-scale distance resolution. Edenhofer et al. (2023) released the differential extinction per parsec,  $E_{XP}$ , measured in an arbitrary reddening unit based on Zhang et al. (2023), which we integrated to the appropriate distance for each cluster. For all stars beyond 1.25 kpc (H Persei, M 37, NGC 1817, NGC 6819, NGC 6866), we used extinctions from the Green et al. (2019) 3D dust map ( $E_{B19}$ ), which are measured in an arbitrary reddening unit and can be converted to extinction in the Pan-STARRS and 2MASS passbands using the coefficients in their Table 1.

To convert the arbitrary reddening from Edenhofer et al. (2023) and Green et al. (2019) to  $E(B - V)$ , we used the following:

$$E(B - V) = 0.829 \times E_{XP} \quad (1)$$

$$E(B - V) = 0.88 \times E_{B19} \quad (2)$$

Eqn. (1) is derived from the combination of  $\frac{E_{SFD}}{E_{XP}} = 0.938^2$  and  $\frac{E(B-V)}{E_{SFD}} = 0.884$  from Schlafly & Finkbeiner (2011), where  $E_{XP}$  is the Zhang et al. (2023) extinction adopted in Edenhofer et al. (2023) and  $E_{SFD}$  is the reddening unit based on the 2D dust emission map from Schlegel et al. (1998). Eqn. (2) is derived from combining  $E(g-r) = 0.901 \times E_{B19}$  (Eqn. 30 from Green et al. 2019) with  $E(B-V) = 0.98 \times E(g-r)$  from Schlafly & Finkbeiner (2011). Once we obtained  $E(B-V)$ , we converted that to  $A_V$  using a differential reddening value of  $R_V = 3.1$ , and converted  $A_V$  to extinction in the Gaia bands  $A_G$ ,  $A_{GBP}$ , and  $A_{GRP}$  using Table 3.1 from Wang & Chen (2019).

We used the Gaia DR3 R.A. and Decl. values to query the dust maps using the `dustmaps`<sup>3</sup> package from Green (2018). We sampled 10 distances for each star from a normal distribution in parallax, after applying zeropoint corrections using `gaiadr3_zeropoint` (Lindgren et al. 2021). For DR3 sources having a relative parallax error of  $\geq 20\%$ , we instead sampled from a normal distribution in distance representative of the stars in the same cluster having  $\geq 20\%$  fractional parallax error. We also sampled extinctions from each dustmap, and propagated these uncertainties in distance and extinction through the conversions in Eqns. (1) and (2) to get our de-reddened uncertainties. Figure 3 shows the final distribution of these  $(BP - RP)_0$  uncertainties, truncated at 0.2 mag for ease of visualization.

Here we note that for stars covered by both the Edenhofer et al. (2023) and Green et al. (2019) dustmaps, there are systematic differences in the measured extinctions. The impact of this is investigated in §6 and Appendix G.1.

### 2.3. Cluster membership

The HDBScan cluster membership probabilities computed by Douglas et al. (2024) are available for 79% of the total number of catalog stars across 27 of our clusters; the percentage per cluster varies. HDBScan was not used for Hyades, Taurus, or Upper Scorpius/ $\rho$  Ophiucus because these are all dispersed in the sky; therefore (i) they would require computationally expensive cone searches, and (ii) the assumption of strong parallax and proper motion definition breaks down, and these associations would require additional treatment. For all stars without HDBScan values, we use the membership probabilities from the source catalogs where available,

and otherwise assign default values according to how the cluster membership was derived (see Appendix E).

HDBScan membership probabilities are heavily dependent on the hyperparameters used, so these introduce a systematic uncertainty in our catalog. However, we find that the overall impact on our model is negligible (see §6).

### 2.4. Cluster ages

We used four literature catalogs as our primary sources for cluster ages: Gaia Collaboration et al. (2018) (hereafter G+18), Bossini et al. (2019) (hereafter B+19), Cantat-Gaudin et al. (2020) (hereafter CG+20), and Long et al. (2023) (hereafter L+23). Each study implemented PARSEC isochrones to fit for cluster properties. We use the average ages across the four catalogs as the fiducial age for each cluster.

The exceptions to the above are the young associations Taurus and Upper Scorpius, and the young cluster  $\rho$  Ophiucus. L+23 compiled rotation periods from all three, and Rebull et al. (2018) compile rotation periods from the latter two. Some rotators assigned to Upper Scorpius by L+23 are assigned to  $\rho$  Ophiucus by Rebull et al. (2018), and vice versa. However, we ignore these designations and instead use the subgroups and corresponding ages from Ratzenböck et al. (2023). Similarly, we break the group of Taurus rotators compiled by L+23 into the sub-groups defined by Krolkowski et al. (2021), and use those ages.

We also conducted a literature review of other age estimates for our clusters, which are summarized in Figure 4 and Table 2. As an example of the variation among studies, Figure 5 presents all age estimates for .

Field Name	Description
Cluster	Name of the star cluster.
Source	Paper in which the age estimate was calculated.
Methodology	The method used to estimate the age of the cluster.
Details	Family of isochrones used to estimate the age (where applicable).
Age (Myr)	The cluster's age in millions of years.

**Table 2.** This table contains the cluster age estimates summarized in Figure 4. The full version is available online in machine-readable format.

<sup>2</sup> Ratio derived from comparing the  $E_{XP}$  reddening and the  $E_{SFD}$  reddening at high latitudes (Xiangyu Zhang 2024, private communication), where the two estimates are expected to agree.

<sup>3</sup> <https://github.com/greggreen/dustmaps>

## 3. AGE INFERENCE FRAMEWORK

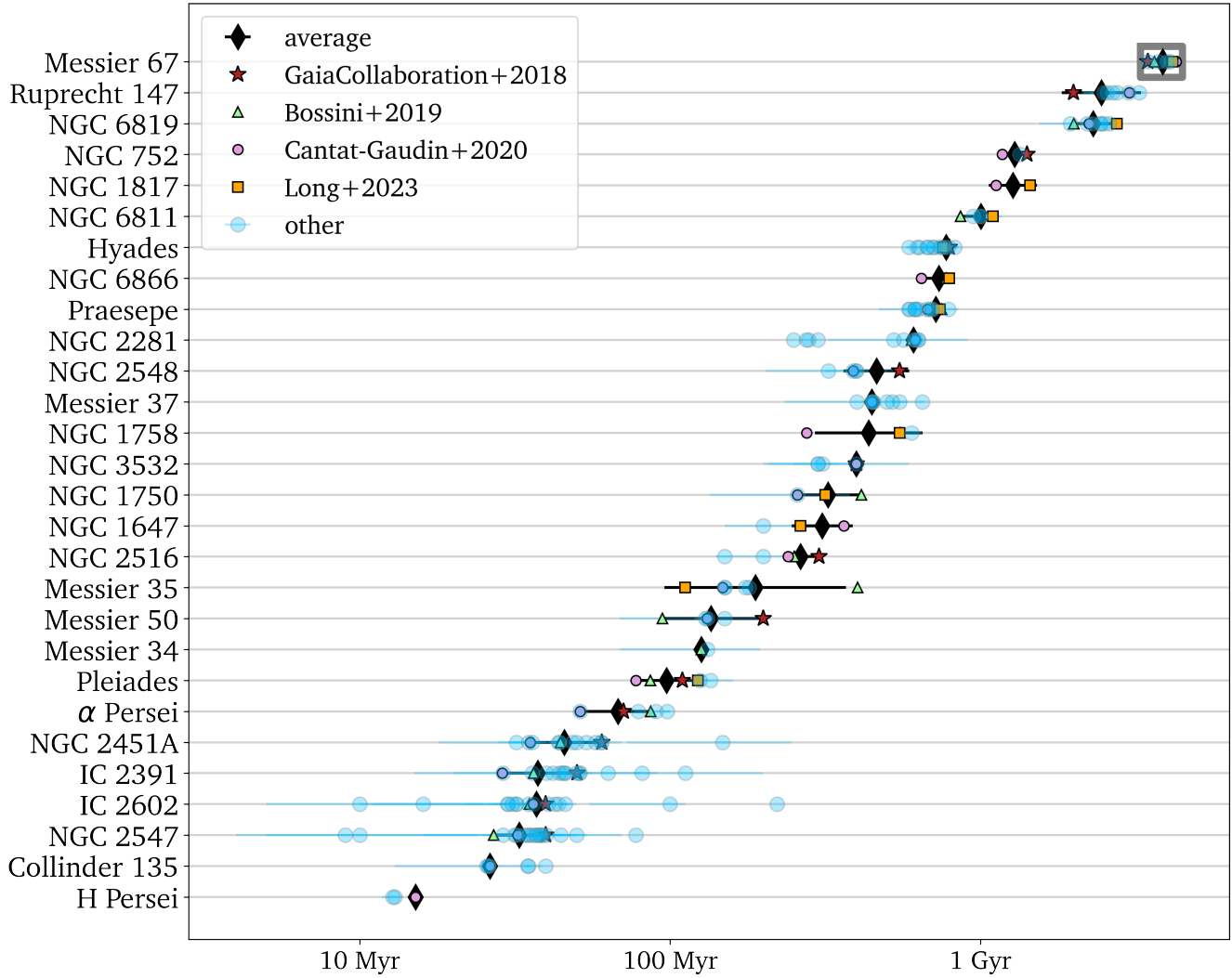


**Figure 4.** Literature age estimates for our clusters, demonstrating the coverage in our catalog. The values from the four main catalogs are highlighted explicitly as red, green, pink, and orange points, and the average value is shown as a black diamond (with an error bar showing the standard deviation across the four catalogs). Other literature estimates are shown as translucent blue circles (see Figure 5 as an example). We exclude the subgroups of Taurus and Upper Scorpius/ $\rho$  Ophiucus from this plot.

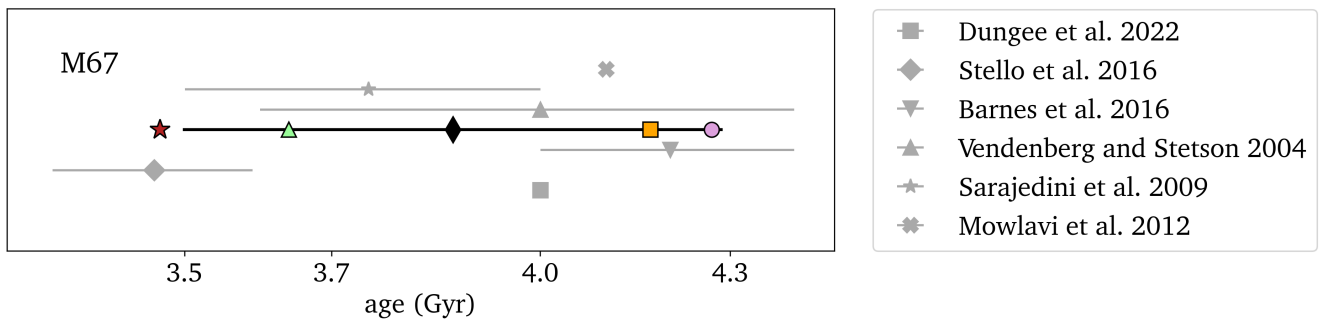


**Figure 5.** A zoomed in view of M67 from Figure 4. Age estimates from all sources are shown here in detail, and jittered vertically for ease of visualization.



To use our data catalog in a statistically robust way, we developed a Bayesian framework to describe the inference of stellar ages ( $\tau$ ) given rotation period ( $P_{rot}$ ), de-reddened DR3 color (described as  $C_0 = BP_0 - RP_0$ ), and photometric uncertainty ( $\sigma_{C_0}$ ). In this context, we have implemented Bayes' theorem as:

$$\mathcal{P}(\tau | P_{rot}, C_0, \sigma_{C_0}) = \frac{\mathcal{P}(P_{rot}, C_0 | \tau, \sigma_{C_0}) \cdot \mathcal{P}(\tau | \sigma_{C_0})}{\mathcal{P}(P_{rot}, C_0 | \sigma_{C_0})} \quad (3)$$

We have chosen to include  $\sigma_{C_0}$  as an independent parameter for ease of computation, but it would also be possible to incorporate it directly within the characterization of  $C_0$ ; both strategies ensure that the impact of color uncertainty is included. We condition all parts of our model on  $\sigma_{C_0}$ , so do not assume any prior on that parameter.

In (3), we can expand  $\mathcal{P}(P_{rot}, C_0 | \tau, \sigma_{C_0})$  as:

$$\mathcal{P}(P_{rot}, C_0 | \tau, \sigma_{C_0}) = \mathcal{P}(P_{rot} | C_0, \sigma_{C_0}, \tau) \cdot \mathcal{P}(C_0 | \sigma_{C_0}, \tau) \quad (4)$$

so that our full equation is:

$$\mathcal{P}(\tau | P_{rot}, C_0, \sigma_{C_0}) = \frac{\mathcal{P}(P_{rot} | C_0, \sigma_{C_0}, \tau) \cdot \mathcal{P}(C_0 | \sigma_{C_0}, \tau) \cdot \mathcal{P}(\tau | \sigma_{C_0})}{\mathcal{P}(P_{rot}, C_0 | \sigma_{C_0})} \quad (5)$$

We choose to separate the likelihood from the priors in this way so that our model learns the  $P_{rot}$  distribution *conditioned* on the other parameters, and not the overall  $P_{rot}$  distribution. By doing so, *we mitigate the influence of selection effects in color and age*, and so minimize the impact of observational biases on our age inference.

With our framework in this form, we can evaluate each term on the right independently.  $\mathcal{P}(P_{rot}, C_0 | \sigma_{C_0})$  in the denominator is the evidence term: this is the integral of the numerator over all possible parameters, and represents the overall likelihood of our observations given our model. Since we are only using a single model, the evidence is a constant scaling term, and the actual value does not matter since we normalize our posteriors to integrate to 1.  $\mathcal{P}(\tau | \sigma_{C_0})$  and  $\mathcal{P}(C_0 | \sigma_{C_0}, \tau)$  are the priors.  $\mathcal{P}(\tau | \sigma_{C_0})$  is defined by:

$$\mathcal{P}(\tau | \sigma_{C_0}) \sim \mathcal{U}[1, 13800] \text{ Myr} \quad (6)$$

While this represents the expected distribution of  $\tau$  conditioned on  $\sigma_{C_0}$ , the age of a star does not physically depend on color uncertainty in any way, so we apply a uniform age prior extending from 1 Myr to the age of the universe.

To build the  $\mathcal{P}(C_0 | \sigma_{C_0}, \tau)$  prior, we firstly assume that the observed colour  $C_0$  does not depend on the age

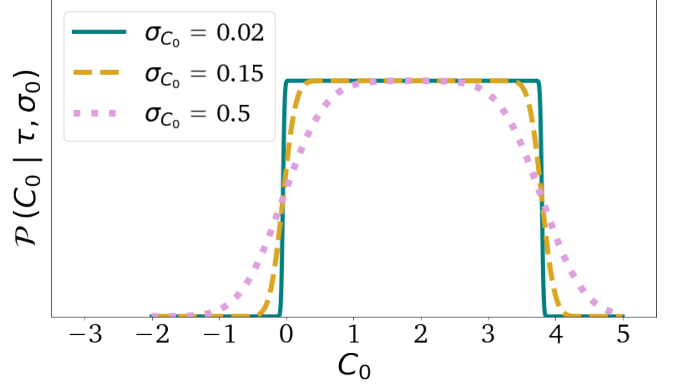


**Figure 6.** A comparison of the distribution described in Eqn. (8) for different values of  $\sigma_{C_0}$ . Larger  $\sigma_{C_0}$  results in a wider, smoother prior around the expected  $C_0$  limits.

of a star. While this is not strictly true (the bluest stars turn off the MS relatively quickly and therefore are more likely to be younger), our model is designed to optimize the *conditional* distribution of rotation period, so we ignore this effect and assume:

$$\mathcal{P}(C_0 | \tau) \sim \mathcal{U}[-0.05, 3.8] \quad (7)$$

The limits of -0.05 and 3.8 are chosen based on the de-reddened colors we expect to see in our catalog with 0 photometric error.

We incorporate  $\sigma_{C_0}$  by convolving (7) with a Gaussian of variance  $\sigma_{C_0}^2$ , so that the functional form of our prior is:

$$\mathcal{P}(C_0 | \tau, \sigma_{C_0}) \sim \mathcal{U}[-0.05, 3.8] * \mathcal{N}(0, \sigma_{C_0}) \quad (8)$$

which effectively sums the two probability distributions on the right. Figure 6 illustrates Eqn. (8) as the change in our  $C_0$  prior as a function of  $\sigma_{C_0}$ . As expected, when  $\sigma_{C_0}$  is small the uniform  $C_0$  distribution dominates, but as  $\sigma_{C_0}$  increases the prior becomes more Gaussian.

#### 4. CHRONOFLOW

Here we introduce **ChronoFlow**, which models the dependence of rotational evolution on age, observed color, and photometric uncertainty by approximating:  $\mathcal{P}(P_{rot} | C_0, \sigma_{C_0}, \tau)$ . **ChronoFlow** implements a conditional normalizing flow (CNF): a neural network-based probabilistic model that excels at modeling complex density distributions.

We trained **ChronoFlow** to learn  $\mathcal{P}(P_{rot} | C_0, \sigma_{C_0}, \tau)$  using the **zuko**<sup>4</sup> framework, a python-based package that implements CNFs using the **PyTorch**<sup>5</sup> deep learning library. In particular, we used a Neural Spline Flow

<sup>4</sup> <https://zuko.readthedocs.io/stable/>

<sup>5</sup> <https://pytorch.org/>

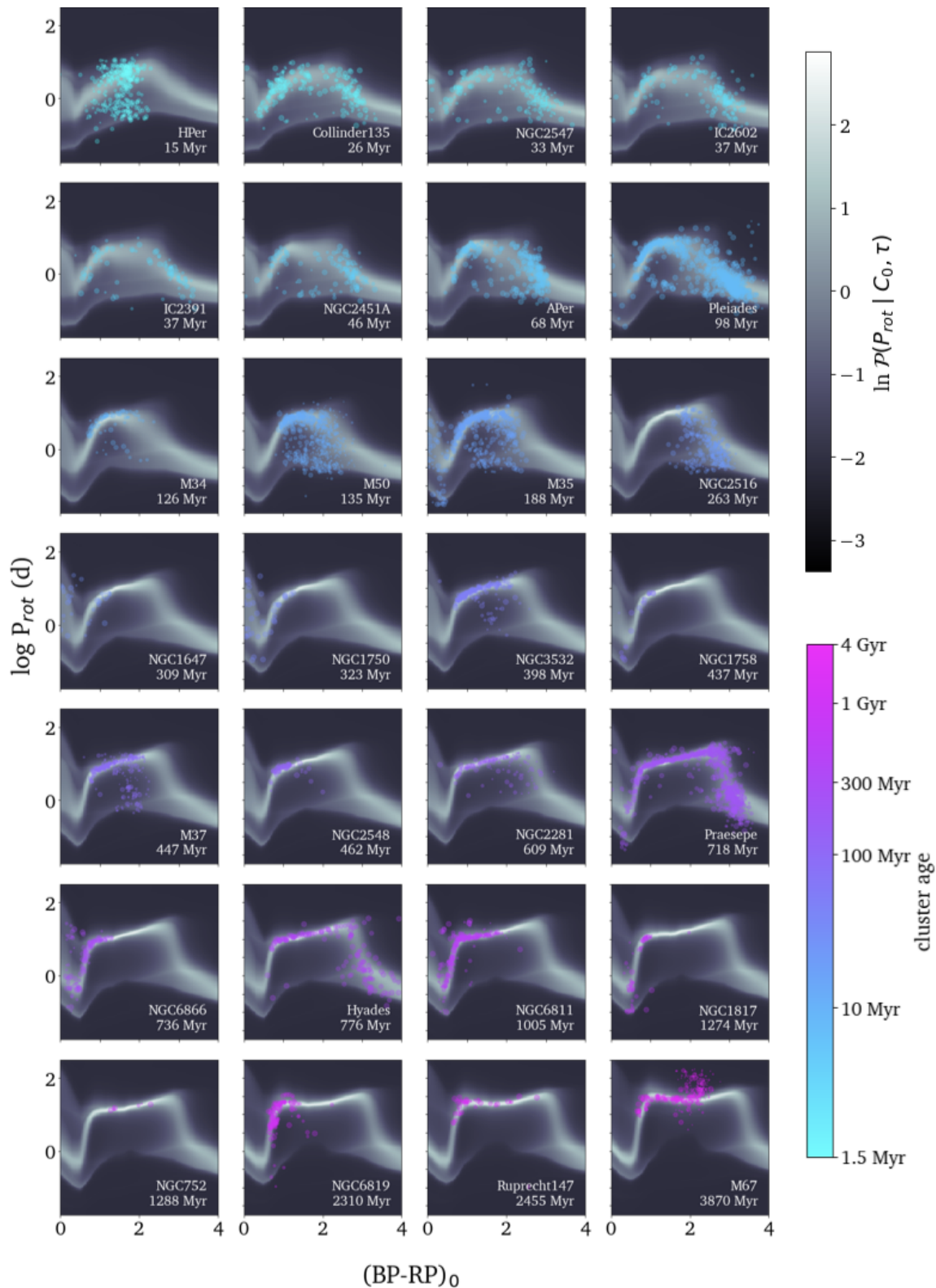


**Figure 7.**  $\mathcal{P}(P_{rot} | C_0, \sigma_{C_0}, \tau)$  (background shading) from ChronoFlow at each cluster's fiducial literature age. Observations from our catalog are plotted as circles (sized by cluster membership probability). We calculate this using representative values for  $\sigma_{C_0}$  and  $p_{cl}$  of 0.028 (the median across our entire catalog) and 0.9 respectively.

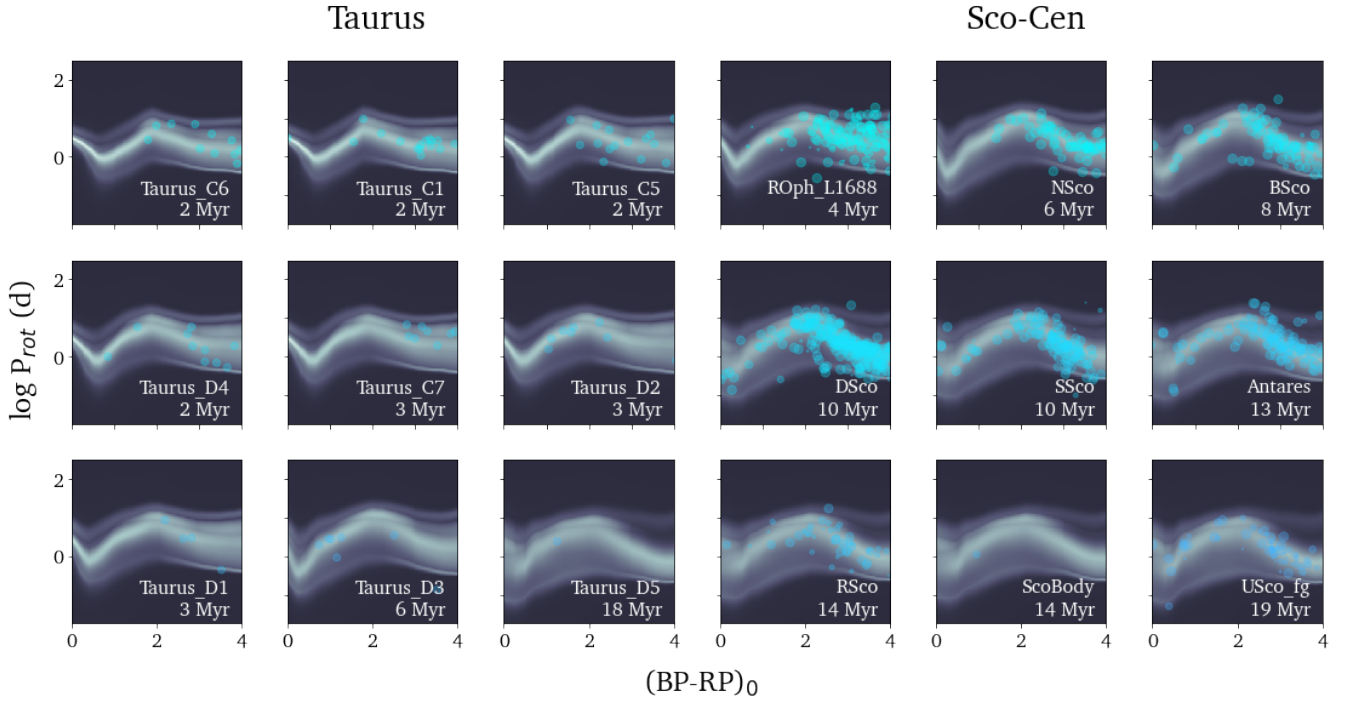


**Figure 8.** Analogous to Figure 7 but for the subgroups of Taurus and Sco-Cen. The rotational sequences are less defined at these younger ages, as the initial dispersion in rotation period dominates. These subgroups are also much closer in age than the clusters in Figure 7, and some are poorly populated.

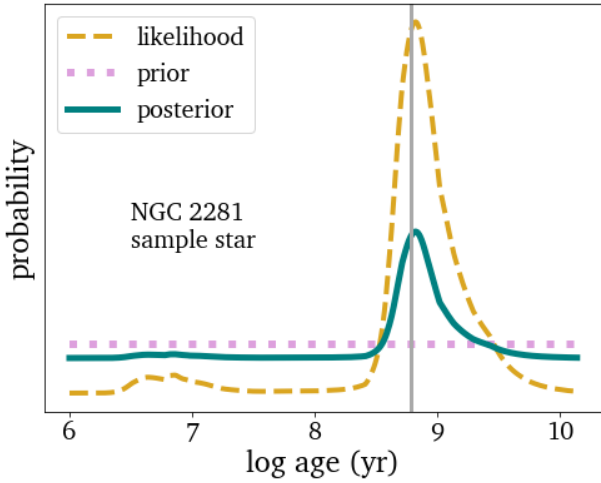


**Figure 9.** Age probability distributions for a sample star from the NGC 2281 cluster ( $\log \tau = 9.1$ ,  $P_{rot} = 10.6$  d,  $C = 0.88$ ). The posterior is clearly likelihood-driven but also smoothed out by the prior, and peaks at an age slightly older than the fiducial cluster age (vertical grey line).

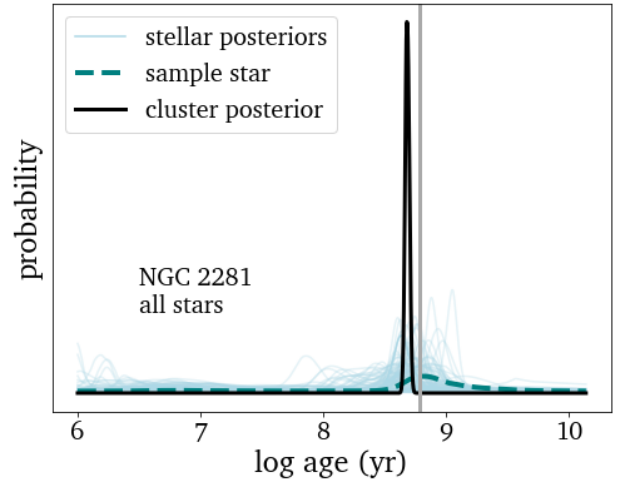


**Figure 10.** Cluster age posterior for NGC 2281. The stellar posterior from Figure 9 is plotted here for reference. The fiducial cluster age is plotted as the vertical grey line. Multiplying the individual stellar posteriors together results in a sharply peaked cluster posterior; in this case it slightly underestimates the fiducial cluster age.

(Durkan et al. 2019) with three transform layers and eight bins, trained for 5,000 epochs. We varied our learning rate using a combination of exponential decay (calibrated to decrease from  $1\text{e-}3$  to  $5\text{e-}7$  over 5,000 steps) and a cosine annealing function with a 1,000-epoch period (see Loshchilov & Hutter 2017). This setup was the result of optimizing the model architecture and hyperparameters, such as learning rate and number of transform layers.

To train ChronoFlow, we used a loss function  $\mathcal{L}$  that minimizes the negative log probability of the conditional distribution:  $\mathcal{P}(P_{rot} | C_0, \sigma_{C_0}, \tau)$ . We further decomposed this probability into two components: the  $\mathcal{P}_f$  computed by our flow, and a uniform background probability  $\mathcal{P}_b$ .  $\mathcal{P}_f$  represents the probability density expected from single stars in a cluster following standard spin-down.  $\mathcal{P}_b$  is included to account for any non-cluster contaminants. We apply  $\mathcal{P}_b$  as:

$$\mathcal{P}_b(P_{rot}) \sim \begin{cases} \frac{1}{P_{rot}^{max} - P_{rot}^{min}} & P_{rot}^{min} < P_{rot} < P_{rot}^{max} \\ 0 & \text{otherwise} \end{cases} \quad (9)$$

where  $P_{rot}^{min}$  and  $P_{rot}^{max}$  are the limits of  $\log P_{rot}$  (in days) over which we evaluate the loss; we use -1.75 to 2.5 to accommodate all observational data. Defining  $w_f$  as the weighting of our NF probability against our background probability, our loss function is (given data for each  $i^{th}$  star out of  $n$  total stars):

$$\mathcal{L} = \sum_{i=1}^n [ -\ln(w_f \cdot \mathcal{P}_f(P_{rot,i} | C_{0,i}, \sigma_{C_{0,i}}, \tau_i) + (1 - w_f) \cdot \mathcal{P}_b(P_{rot,i})) ] \quad (10)$$

We also break down our weighting  $w_f$  into:

$$w_f = (1 - p_{out}) \cdot p_{cl} \quad (11)$$

Here,  $p_{cl}$  is the cluster membership probability for each star (as described in §2), and  $p_{out}$  is a universal ‘‘outlier probability’’ of 0.05.  $p_{out}$  represents the probability of cluster member straying from the single star rotational sequence (e.g., a blue straggler or an unresolved binary). In future phases, applying a dynamic outlier probability per star that uses indications of binarity (such as radial velocity) could further improve this model.

## 5. RESULTS

Figures 7 and 8 present the conditional probability densities calculated by ChronoFlow at the fiducial ages of each of our clusters, including the location of each cluster members in  $P_{rot} - C_0$  space for reference. An important note is that the ‘‘high’’ probabilities in regions of sparse data at the color extremes are due to the *conditional* nature of our model. Since each subplot

represents  $p_f(P_{rot} | C, \sigma_{C_0}, \tau)$  at a single age, the probability distribution along any vertical line will integrate to 1. Hence, these ‘‘wings’’ represent the  $p_f(P_{rot})$  distribution that we would expect to see given stars at those ages and colors, not where we would expect to see a high density of stars overall. *This illustrates the importance of applying a conditional normalizing flow to mitigate selection effects*, which otherwise could bias our NF in color space.

To quantitatively measure how well the probability densities from ChronoFlow match observations, a benchmark metric was required. We chose to use the average stellar log probability:  $p_{*,avg} = \mathcal{P}(P_{rot}, C_0 | \sigma_{C_0})$ , i.e. the evidence term in Eqn. (3). Clusters with stars concentrated in the high probability regions will have a higher  $p_{*,avg}$ , and those with more stars outside of those regions will have a lower  $p_{*,avg}$ . We use the average probability instead of total probability to account for the different sample size of each cluster. With this metric, we conducted two benchmark tests: (i) a cluster-by-cluster comparison, and (ii) an assessment of  $p_{*,avg}$  for our observational data against  $p_{*,avg}$  of a simulated data set. The details of these tests are described in Appendix F; overall we find that *ChronoFlow fits observations with high accuracy*.

### 5.1. Stellar and cluster age recovery

Evaluating Eq. (5) over a grid of ages, for a constant set of observed parameters, is straightforward, and this generates a posterior age probability for each star. Figure 9 presents an example of this. As expected, given the almost uniform prior, the posterior follows the likelihood closely.

To obtain the posterior age estimation for a cluster  $\mathcal{P}(\tau_{cl})$ , we take the product of the individual stellar posteriors for all  $n_{cl}$  stars in the cluster:

$$\mathcal{P}(\tau_{cl}) = \prod_{i=1}^{n_{cl}} \mathcal{P}(\tau_i | P_{rot,i}, C_{0,i}, \sigma_{C_{0,i}}) \quad (12)$$

When calculating these cluster posteriors, we exclude stars having  $C_0 \lesssim 0.3$  because the stability of our model suffers in this regime. The reason for this behavior is likely twofold: (i) we have sparse sampling; and (ii) those stars may predominantly be above the Kraft break (Kraft 1967), meaning they have radiative envelopes and do not undergo magnetic braking. Beyer & White (2024) identify the Kraft break at  $(BP - RP)_0 \approx 0.54 - 0.60$ , indicating that  $C_0 = (BP - RP)_0 = 0.3$  is a conservative cut and should not exclude any useful data.

As a cluster age recovery exercise, we applied our trained model to Eqn. (5) using leave-one-out cross val-

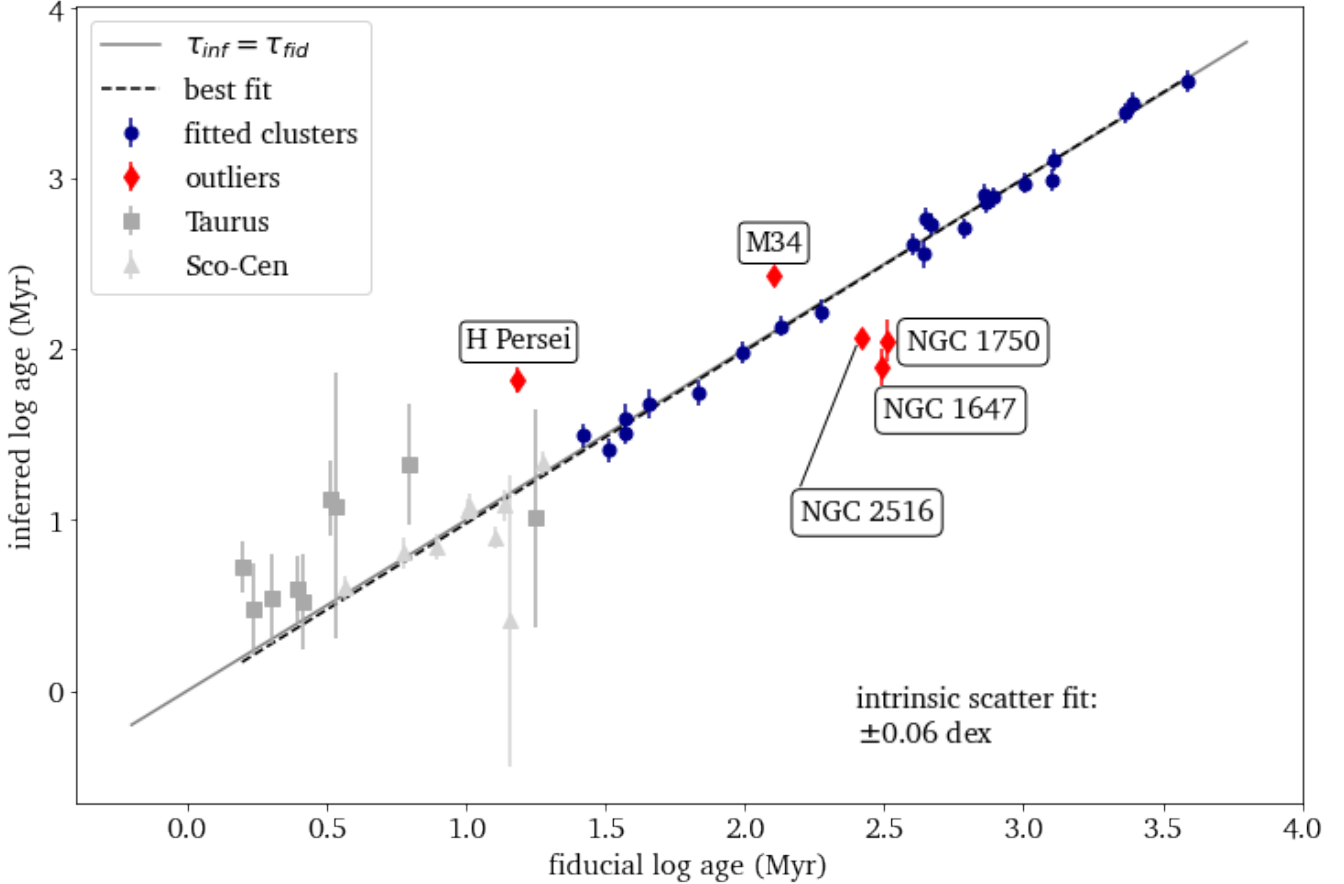


**Figure 11.** Inferred cluster ages from LOOCV compared to the fiducial values from literature. Subgroups of the Taurus and Sco-Cen regions are plotted in grey, and the five anomalous clusters are plotted in red. The best fit line is  $\tau_{\text{inf}} = (1.01 \pm 0.02) \cdot \tau_{\text{fid}} - (0.03 \pm 0.06)$ , with an intrinsic scatter of 0.06 in  $\tau_{\text{inf}}$ . This indicates that there is *no systematic offset* in  $\tau_{\text{inf}}$  resulting from the model itself. Error bars include both the statistical uncertainty for each cluster estimate and the intrinsic scatter.

idation (LOOCV), where each cluster age was inferred using a model that *excluded* the cluster from training. Figure 11 presents these ages compared to the fiducial literature values. There is very good agreement, aside from five outliers. Excluding those five clusters, we fit a line to the  $\tau_{\text{inf}}$  vs.  $\tau_{\text{fid}}$  relationship using `emcee`<sup>6</sup> (Foreman-Mackey et al. 2013). We included a free parameter for intrinsic scatter, which we found to be 0.06 dex. Given that the statistical uncertainty in the individual cluster posteriors (median of 0.016 dex) is therefore dominated by the intrinsic scatter, we conclude that *ChronoFlow can infer cluster ages to an overall statistical uncertainty of 0.06 dex, or  $\approx 15\%$* . Since these results are from our LOOCV exercise, each estimate is *simulating a scenario where our model is encountering new data*, so this is the level of accuracy we would expect from *ChronoFlow* applied to new popula-

tions. We do not expect precise age estimations for the subgroups of Taurus and Sco-Cen, since they generally have limited data and stars at such young ages have large  $P_{\text{rot}}$  dispersion. We see a clear systematic where Taurus ages are overestimated, but nevertheless *ChronoFlow* recovers the young sungroup ages to within uncertainties reasonably well.

### 5.1.1. Outliers

We investigated the five anomalous clusters further. Figure 12 presents the observed data for those clusters plotted against our flow results at: (i) the fiducial literature age, and (ii) the age that the final version of *ChronoFlow* (from which we exclude these five clusters during training) infers. It is clear that for H Persei, the model prediction at the fiducial age is a better visual fit than our inferred age. So, we consider this an outlier that our model is not able to characterize well. In contrast, the other four clusters generally *appear* to be better visual fits to our inferred ages. We therefore

<sup>6</sup> <https://emcee.readthedocs.io/en/stable/>

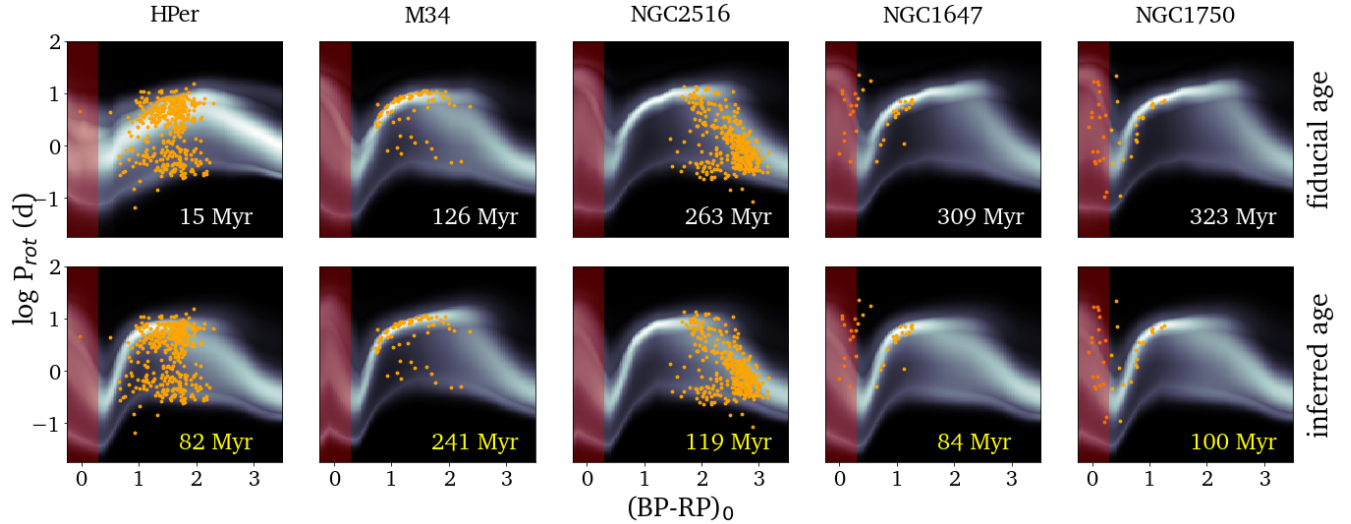


**Figure 12.** A comparison of the five anomalous clusters from Figure 11. Observed data are plotted over our model’s probability density at both fiducial (top) and inferred (bottom) cluster ages. The same default parameters for  $\sigma_{C_0}$  and  $p_{cl}$  were used as in Figure 7. We exclude stars having  $(BP - RP)_0 \leq 0.3$  from our age inference, and have shaded this region in red.

present our inferred ages for these four clusters as new cluster age estimates:

- **M34:**  $241^{+39}_{-33}$  Myr
- **NGC 2516:**  $119^{+21}_{-18}$  Myr
- **NGC 1647:**  $84^{+24}_{-16}$  Myr
- **NGC 1750:**  $100^{+31}_{-21}$  Myr

These uncertainties include both the statistical uncertainty for each cluster and the intrinsic scatter of our model.

### 5.2. Age recovery for single stars

Our focus to this point has been on characterizing the rotational evolution of a population of stars, but now we examine individual stars. As a standalone test, we applied ChronoFlow to the Sun using  $P_{rot} = 26.09$  days and  $(BP - RP)_0 = 0.817$  (from Popinchalk et al. 2021), and calculated its age to be  $5.1^{+1.7}_{-1.4}$  Gyr. This is consistent at  $1\sigma$  with the true age of 4.6 Gyr.

More comprehensively, we conducted another version of LOOCV, but using batches of stars drawn from all clusters instead of testing a single cluster at a time. We divided our data catalog (excluding H Persei, M34, NGC 2516, NGC 1647, and NGC 1750) into 20 batches, and trained 19 different models that each included 19/20 batches (95% of our data). Clusters were distributed as equally as possible between batches to ensure maximal age coverage in each batch. We then used each model to calculate stellar age posteriors for the 5% of stars that were left out of training.

Figure 13 presents these results. The top panel shows the residuals as a function of stellar age, the middle

panel plots the residuals against  $C_0$ , and the bottom panel against measured  $P_{rot}$ . Members of Taurus and Sco-Cen are plotted in grey; we do not expect this model to reliably recover the ages of such young stars.

There is a clear trend at older ages: a dense population of stars that the model estimates well, and a dispersed tail that the model underestimates, which is reflected in the median residual value of  $-0.17$  dex. These “underestimated” stars are those in the wide distribution of fast rotators in their cluster, as confirmed from the lower panel where these stars generally have an intermediate rotation period of  $\approx 11$ -17 days. The model interprets these as being on a slowly rotating sequence at a younger age.

Overall, 79% of stars have a fiducial age that lies in the  $1\sigma$  credibility interval of our posterior age estimates, so we are *overestimating* the uncertainty on these posteriors. Figure 14 illustrates this systematic. The median  $1\sigma$  uncertainty on the residuals is  $[-0.78, 0.64]$  dex. It is also important to note that there is almost certainly some level of contamination in our cluster sample, and therefore for non-members we are incorrectly using the cluster ages as the true ages of these stars. This effect is difficult to quantify, since by definition the contaminants are not identifiable, so we conclude that the uncertainty on individual stellar age estimates is *conservatively*  $\approx 0.7$  dex.

## 6. SYSTEMATIC UNCERTAINTIES

In §5 we evaluated the statistical uncertainty associated with our age inference. However, there are additional systematic uncertainties that are important considerations for any gyrochronology model. We tested these to

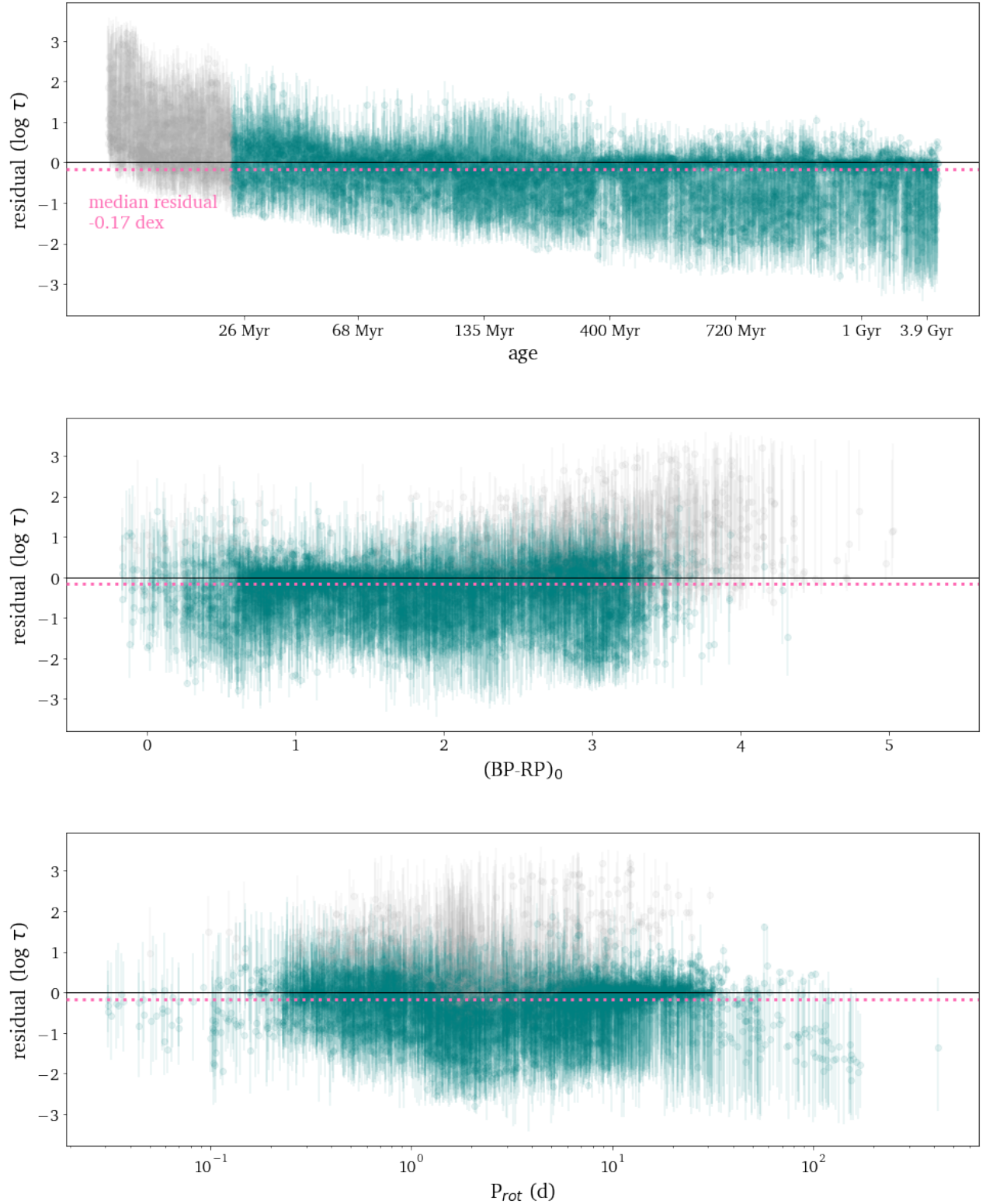


**Figure 13.** Individual stellar age residuals from posterior estimates. Grey stars are members of the Taurus and Sco-Cen associations, and all other clusters are plotted in teal. In the top panel, stars are uniformly distributed along the age axis in order of increasing age, instead of plotted directly against age, for ease of visualization. The error bars encapsulate the 16th to 84th percentiles of every stellar posterior estimate. The black solid line is plotted at a residual of 0, and the pink dotted line is plotted at the median residual over our entire catalog (excluding the Taurus and Sco-Cen members), which is -0.17.

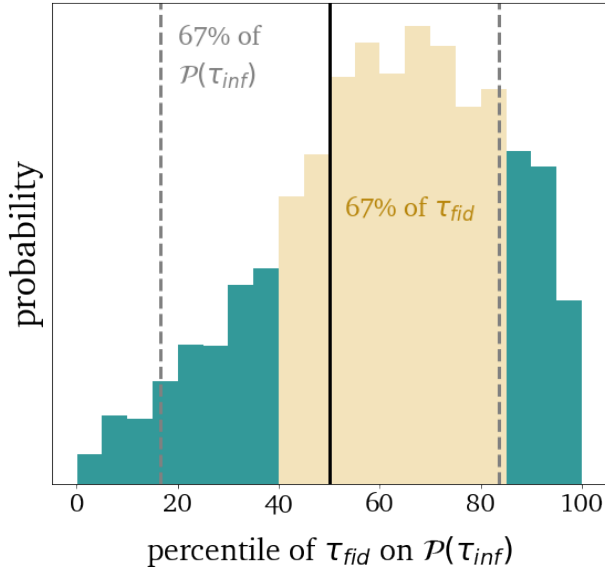


**Figure 14.** Distribution of the percentiles at which  $\tau_{fid}$  lies in each  $\mathcal{P}(\tau_{inf})$  posterior. The posteriors systematically underestimate the fiducial stellar ages, but overestimate the uncertainty. The  $\pm 1\sigma$  error in the posteriors is bounded by the dashed grey lines (the solid black line is the median), and the  $\pm 1\sigma$  distribution of fiducial literature ages  $\tau_{fid}$  is shown as the light yellow region.

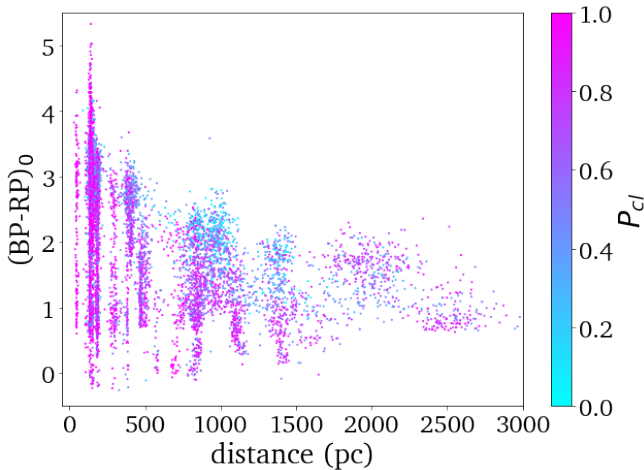


**Figure 15.** HDBScan Cluster membership probabilities as a function of color and distance. As expected, there is weaker confidence in stars that are redder and farther away, since their astrometry is less precise.

understand how important they are to our overall error budget:

- **De-reddening.** The choice of dustmap used to derive stellar extinctions directly affects photometric color. We analyze this in two ways, by: (i) characterizing the inherent deviation caused by using different dustmaps for both training and infer-

ence, and (ii) predicting ages using photometry from a different dustmap than was used to calibrate the model. The impact of the former is relatively small, but the impact of the latter can be significant. Details are provided in Appendix G.1.

- **Cluster membership cuts.** We analyze the impact of cluster membership cuts by comparing predictions for three clusters derived from three different data catalogs for each cluster: the Pleiades, Praesepe, and NGC 6811. Details are provided in Appendix G.3. The impact of this was negligible.
- **Source survey.** We test for hidden systematics by evaluating our age inference both with and without ground based data in our training catalog. Including those data improves our age recovery and does not introduce additional systematic uncertainty, indicating that they add value to our catalog. Details are provided in Appendix G.2.
- **Calibration ages.** Since cluster ages are inherently model-dependent, the choice of model calibration ages affects age inference. We examine this impact using a variety of training ages, and find this to be a significant systematic.
- **Bias in  $p_{cl}$ .** Since HDBScan cluster membership probabilities are reliant on Gaia astrometry, they are fundamentally biased lower towards fainter (i.e. redder and more distant) stars which have larger astrometric errors. Figure 15 illustrates this. Additionally, since HDBScan results are heavily dependent on the hyperparameters, it is important to quantify how that impacts age inference.

We summarize our results for these systematics in Table 3. The results of the space vs. ground based survey test indicated that there was no quantifiable systematic, so that is not included.

While the effect of the bias in  $p_{cl}$  with distance and color cannot be reliably quantified, qualitatively this results in wider distributions of  $\mathcal{P}(P_{rot} | C_0, \sigma_{C_0}, \tau)$  in that regime, due to the increased weighting of the uniform background probability  $\mathcal{P}_b$ . We test the influence of  $p_{cl}$  on our model by comparing LOOCV results using HDBScan probabilities against LOOCV results using  $p_{cl}$  from the source catalogs. The difference in cluster posteriors, outliers, and intrinsic scatter is negligible, indicating that this systematic is insignificant.

### 6.1. Other considerations

Another attribute that may affect rotational evolution is metallicity. It would be straightforward to include



Metric	Description	Value (dex)
$\sigma_{A,1}$	Systematic uncertainty due to choice of dust map in de-reddening.	0.01
$\sigma_{A,2}$	Systematic uncertainty resulting from different de-reddening processes between calibration photometry and prediction photometry.	$\lesssim 0.04$
$\sigma_{cl}$	Systematic uncertainty caused by varying cluster membership criteria.	0.01
$\sigma_{\tau,cal}$	Systematic uncertainty due to varying the model calibration age.	$\approx 0.04$

**Table 3.** Summary of our systematic test results. The dominant sources of uncertainty come from using different extinctions for training and inference, and the model-dependency of calibration ages themselves. Added in quadrature, these result in a total systematic uncertainty of  $\approx 0.06$  dex.

metallicity as a training parameter in our model, however most of the open clusters are approximately solar metallicity since they are nearby. Given this lack of parameter space coverage combined with the uncertainties on measurements, we do not expect our model to learn anything meaningful from including metallicity. Should significant rotation data become available for stars with super- or sub- solar metallicity, this would be worth investigating.

Another consideration is how to optimize this framework for the lowest mass (e.g. K and M) stars. In that regime, we would expect the Gaia  $(G - RP)_0$  color to be more descriptive than  $(BP - RP)_0$  given the low flux in the BP band, so including both as training parameters could improve performance.

## 7. APPLICATIONS

### 7.1. New cluster ages

In addition to generating new age estimates for M34, NGC 2516, NGC 1647, and NGC 1750 as described in §5.1, we applied our model to two systems that were not part of our data catalog: the NGC 6709 open cluster (using rotation periods from Cole-Kodikara et al. 2023), and the Theia 456 stellar stream (using rotation periods from Andrews et al. 2022). Gaia EDR3 IDs were provided in both cases, so we calculated the de-reddened photometric uncertainty using the process described in §2.2 using the Edenhofer et al. (2023) dust map. We retained 162 of the 171 Theia 456 stars having reported rotation periods; one was excluded because the ID provided did not match any records in Gaia DR3 or EDR3, and eight more were excluded because they have Gaia RUWE values  $\geq 1.4$ . For NGC 6709, we retained 34 out of the 48 stars with reported rotation periods. 11 were excluded because they were flagged as binaries by Cole-Kodikara et al. (2023), and none of the 37 remaining had a Gaia RUWE  $\geq 1.4$ , but three also had  $(BP - RP)_0$  values less than 0.3, which we excluded. We then calculated the cluster age posteriors for each, following the

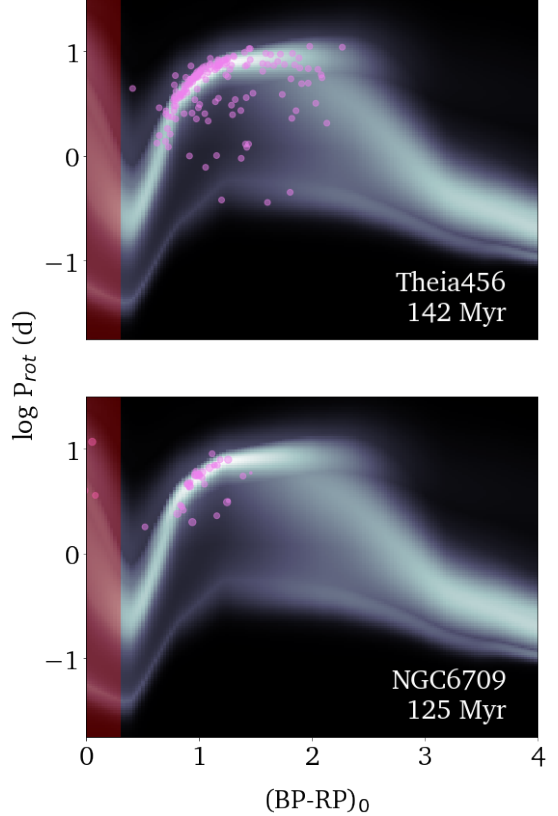


**Figure 16.** A visualization analogous to Figure 7 showing the probability densities generated by our model at our inferred ages for the Theia 456 stellar stream and the NGC 6709 open cluster, along with the observational data. The stars in NGC 6709 are sized according to cluster membership probability; those values were not provided in the Theia 456 catalog so all stars are sized equally (reflective of our fiducial cluster membership probability of 0.9). We exclude stars having  $(BP - RP)_0 < 0.3$  from our age inference, and have shaded this region in red.

methodology described in §5.1 (including the intrinsic scatter in our uncertainties).

We found an age for Theia 456 of  $141^{+31}_{-20}$  Myr. Andrews et al. (2022) found ages for Theia 456 (using both isochrones and gyrochronology) of 150-200 Myr,

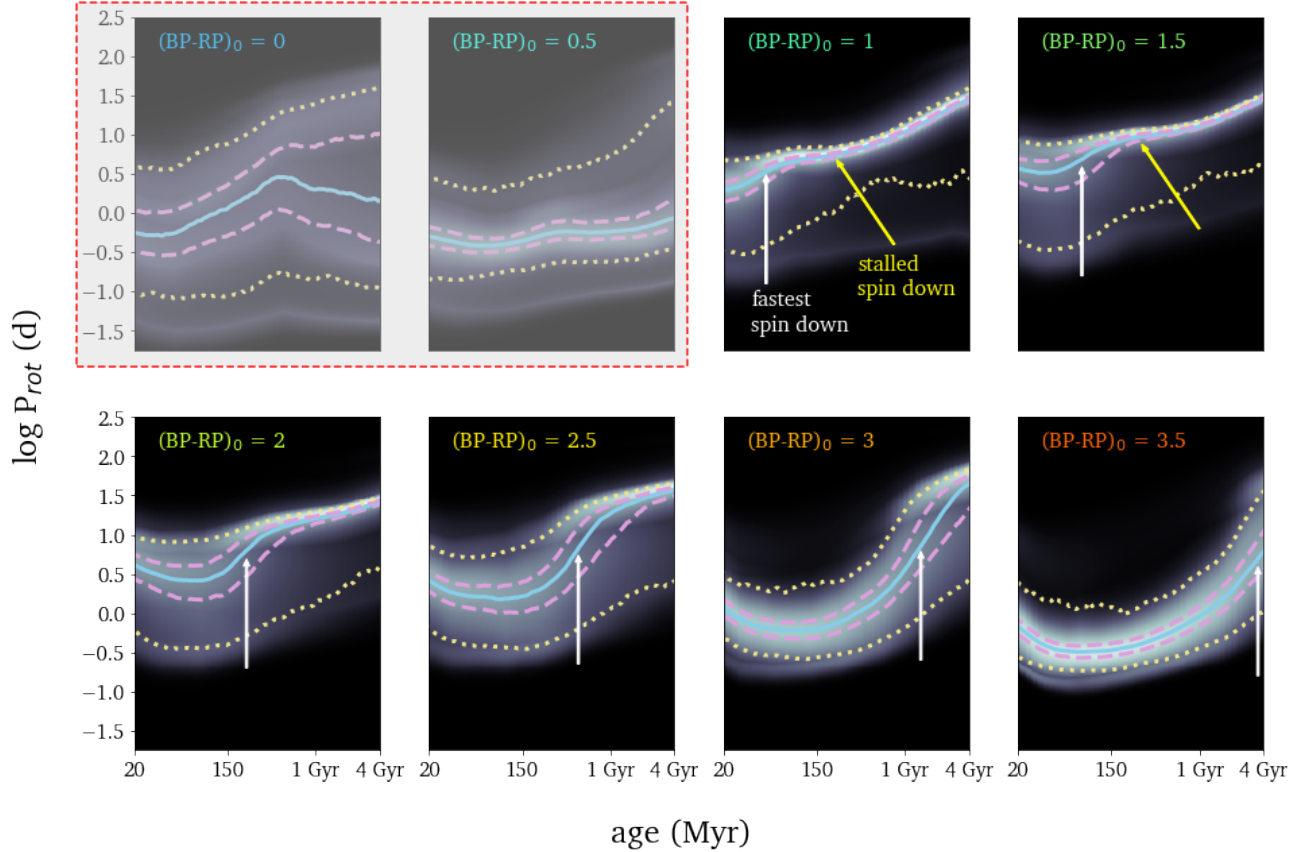


**Figure 17.** “Evolutionary” tracks calculated from our model for eight different  $(BP - RP)_0$  values. The background shading represents the conditional probability density  $\mathcal{P}(P_{rot} | C_0, \tau)$  for a representative  $\sigma_{C_0}$  value of 0.028. Contours represent the 10th, 33rd, 50th, 67th, and 90th percentiles for each panel. We have smoothed the contours for ease of interpretability by averaging across a window of 20 timesteps, which corresponds to a window width of  $\log(\tau) = 0.3$ . The first two panels are greyed out because of limited training data, and expected contamination from stars with radiative envelopes. In each panel, we indicate the approximate age at which the median stars experience their fastest spin down with white arrows. This age is inversely proportional to stellar mass, a ubiquitous trend in literature. We also indicate regions of apparent stalled spin down with yellow arrows.

Name	ChronoFlow Estimate (Myr)	Literature Age Range (Myr)
M34	$241^{+39}_{-33}$	125–250
NGC 1647	$84^{+24}_{-16}$	260–365
NGC 1750	$100^{+31}_{-21}$	250–415
NGC 2516	$119^{+21}_{-18}$	150–300
NGC 6709	$125^{+43}_{-26}$	100–190
Theia 456	$142^{+32}_{-20}$	150–200

**Table 4.** Age estimates from ChronoFlow. All uncertainties include the intrinsic scatter calculated in §5.1. M34, NGC 6709, and Theia 456 are all consistent with literature to  $1\sigma$ , while ChronoFlow infers significantly younger ages for NGC 1647 and NGC 1750.

and Kounkel & Covey (2019) estimated it to be  $165^{+70}_{-50}$

Myr. Our estimate is on the lower end of these literature values, but consistent at  $1\sigma$ .

We calculated NGC 6709 to be  $125^{+43}_{-26}$  Myr. Cole-Kodikara et al. (2023) found a rotational age of  $\approx 150$  Myr for this cluster, but noted that the MS turnoff indicated an older age. They also summarized recent work as supporting ages ranging from 100 to 190 Myr. Again, our estimate is on the lower end compared to these but consistent at  $1\sigma$ .

Figure 16 presents a comparison of the observed data for both systems to the probability density grids from ChronoFlow, analogous to Figure 7. Table 4 summarizes these ages, as well as the four revised cluster ages described in §5.1.1.

Of these six comparisons, the inferred ages of NGC 1647 and NGC 1750 are significantly lower than literature estimates. Both of those clusters have a relatively small sample size in our catalog, and also a dearth of

rotators redder than  $C_0 \approx 1.5$ , which may contribute to this difference. Nonetheless, Figure 12 shows that our inferred ages *do* fit ChronoFlow better than the literature ages.

### 7.2. Rotational ‘evolution’ tracks

Another way that we can examine our data is by looking at the evolution of the  $P_{rot}$  distribution at a static color. This can tell us how we would expect a group of similarly massive stars to evolve over time. Figure 17 presents these results over a  $(BP - RP)_0$  range of 0 to 3.5 (in steps of 0.5). It is important to note that while the contours do not necessarily represent the exact evolutionary paths that a star might take, they are a measurement of the expectation values for  $P_{rot}$  over time in a population.

For  $(BP - RP)_0 = 0$  and 0.5, the expected smooth spindown cause by magnetic braking is not apparent. This may be due to a lack of training data in this regime, and contamination from stars with radiative envelopes (see §5.1).

The tracks at  $C_0 = 1 - 2.5$  exemplify typical spindown behaviour for solar type stars. We see the initial wide distribution in rotation periods converging into a tight sequence of fast rotators, which happens slower for redder stars. Another well feature in rotation evolution is mass-dependent “stalled spin down”. Agüeros et al. (2018) found evidence for this weakened braking between approximately the ages of Praesepe at 650 Myr and NGC 6811 at 1 Gyr, and Curtis et al. (2019) and Douglas et al. (2019) found similar results. We also see this in our model; it manifests as a flattening of the evolutionary tracks seen in Figure 17 at  $C_0 \approx 1 - 2$ .

Examining the reddest stars in our sample, Popinchalk et al. (2021) found that M dwarfs at field ages exhibited a bimodal spin down pattern, with a group of fast rotators having  $P_{rot} \lesssim 2$  days, and another overdensity at  $P_{rot} \gtrsim 60$  days. Pass et al. (2022) found similar results using wide binaries: some M dwarfs converged onto a slowly rotating sequence quickly, but some remained rotating fast for much longer before spinning down quickly. This bimodal spindown is also a feature of solar mass stars in physical models (e.g. Garraffo et al. 2018). The Garraffo et al. (2018) model has not been tested for fully convective M dwarfs yet, since it relies on convective turnover timescale, which has historically been difficult to measure for such stars. However, Gossage et al. (2024) have recently made progress towards a better method for calculating that parameter. The bimodality with fast and slow rotators is somewhat apparent in our model for  $\approx$  solar mass stars, however we do not see the same buildup of fast rotators in the reddest stars. Instead, while we

see a narrow distribution of slow rotators appear at  $\gtrsim 1$  Gyr, the distribution of fast rotators is broad.

From Figure 17, it is apparent that we do not expect convergence onto a slowly rotating sequence to occur over the timescale of our oldest open cluster (M67;  $\approx 4$  Gyr) for the reddest stars having  $C_0 \gtrsim 3$ . Pass et al. (2022) expect spindown for fully convective M dwarfs to occur in 2-3 Gyr. However, it is worth noting here that the delayed spindown in our model may be an artifact of the reddest stars in our sample being observed in Praesepe and Hyades (700-800 Myr), at which age they have not spun down yet. Since our catalog does not include stars having  $(BP - RP)_0 \gtrsim 2.5$  past that age, it may struggle to predict their spindown.

### 7.3. Extrapolation to field ages

Our oldest training stars are  $\approx 4$  Gyr. Many field stars are older than this, so the rotational evolution that ChronoFlow predicts past that age is extrapolation. We leave a detailed analysis for subsequent studies, but here we examine our model behavior qualitatively. Figure 18 presents the extrapolation of  $\mathcal{P}(P_{rot} | C_0, \sigma_{C_0}, \tau)$  to older ages for characteristic color values. The model evolves smoothly past 4 Gyr, and predicts a continuation of the rotational evolution seen at the ages of our older open clusters.

We do not attempt to characterize the behavior at  $C_0 = 0$  or 0.5. For  $C_0 = 1$  to 2, essentially all stars have converged onto a narrow slowly rotating sequence by 4 Gyr, and our model expects them to collectively continue spinning down at field ages. For  $C_0 = 2.5$  to 3.5 (approximately the M dwarf regime), we see the slowest rotators continue to spin down, but also a slight narrowing of the overall distribution of  $P_{rot}$ . This generally aligns with the behaviour of M dwarfs at field ages characterized by Popinchalk et al. (2021) and Pass et al. (2022), where some of these stars continue to rotate rapidly at field ages.

As a simple test of our model’s extrapolation behavior, as described in §5.2, we obtained an age estimate for the Sun of  $5.1_{-1.4}^{+1.7}$  Gyr.

## 8. CONCLUSIONS AND SUMMARY

In this work we constructed a rotational catalog of 7,407 stars, from 28 open clusters plus subgroups of the Taurus and Sco-Cen associations. This is the most comprehensive open cluster rotational catalog to date, spanning an age range of 1.5 Myr to 4 Gyr. We have standardized all photometry to Gaia DR3, which we dereddened using the 3D dustmaps from Edenhofer et al. (2023) and Green et al. (2019). We also propagated uncertainties in parallax, Gaia photometry, and dustmap

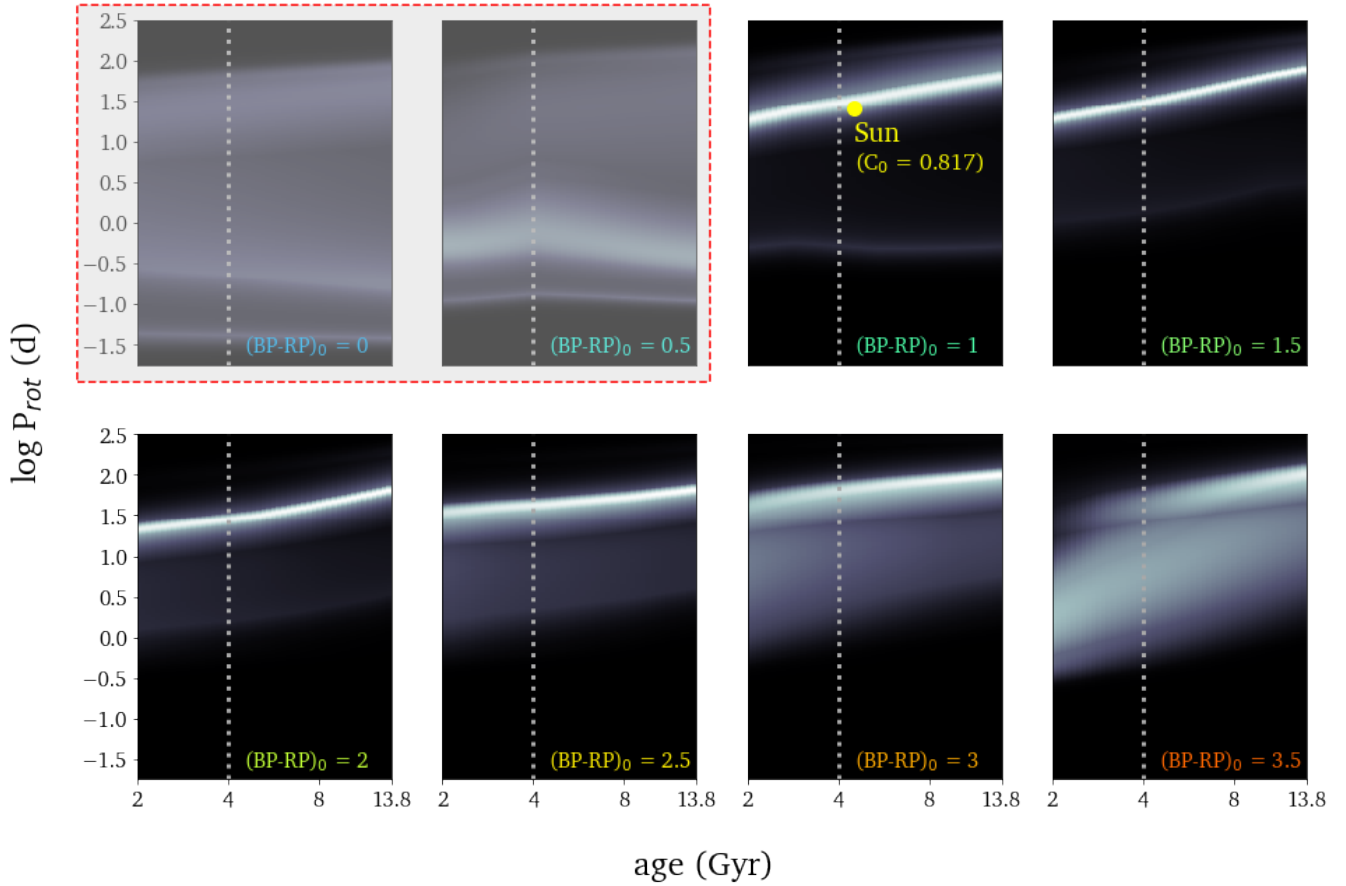


**Figure 18.** Probability densities  $\mathcal{P}(P_{rot} | C_0, \tau)$  extrapolated to the age of the universe for different characteristic  $C_0$  values. The vertical line represents oldest training age (M67). We have plotted the Sun in the third panel for reference, showing that it fits our extrapolated model reasonably well.

extinction to get realistic color uncertainties. Finally, we have included cluster membership probabilities, sourced from literature and HDBScan analysis. We present this catalog as part of this work, as well as a deep literature compilation of age estimates for the clusters in the catalog. We hope that this catalog will be a useful benchmark for gyrochronology, and also for the broader astronomical community.

We used this catalog to develop a completely data-driven gyrochronology model using a conditional normalizing flow: **ChronoFlow**. We trained **ChronoFlow** to learn  $P_{rot}$  probability density distributions conditioned on Gaia DR3 color, photometric uncertainty, and age. By constructing it in this way, *we insulate the model against observational biases in color and age space*. Our model is also the first to use variable cluster membership probabilities per star, which constrains our model more realistically.

We have shown that **ChronoFlow** accurately captures the observed  $P_{rot}$  dispersion, a result which has eluded many theoretical and empirical models to date. Our model can be used to compute the probability density

in color- $P_{rot}$  space at any given age, or examine the  $P_{rot}$  density evolution over time for fixed colors. We have also implemented **ChronoFlow** in a Bayesian framework to *infer stellar and cluster age posterior probabilities*. The uncertainty on individual stellar ages is  $\approx 0.7$  dex, and we can constrain cluster ages with a statistical uncertainty of  $\approx 0.06$  dex, or 15%. As an example of its applicability, we have used **ChronoFlow** to calculate new age estimates for five open clusters and one stellar stream.

Furthermore, we thoroughly tested systematic uncertainties. These includes the effect of mixing dustmaps when calculating stellar extinction, the effect of cluster member selection, a comparison of space vs. ground based surveys, and the variance caused by different families of training ages. We note two dominant sources of systematic uncertainty: (i) the application of different extinction procedures to photometry for training vs. inference, and (ii): the choice of ages in the training dataset. Both of these affect cluster age inference to the order of  $\approx 0.04$  dex, and the total uncertainty arising from all sources of systematics is  $\approx 0.06$  dex. Combined

with the statistical uncertainty of our model, our total uncertainty in population age inference  $\approx$  **0.08 dex**.

To summarize the key outcomes of this work:

- We have developed the most robust open cluster rotational catalog to date, with **standardized Gaia DR3 photometry** de-reddened using 3D dust maps, and **accurate photometric errors**.
- We provide **cluster membership probabilities** for all stars in our catalog.
- We have developed **ChronoFlow**: a data-driven model that accurately predicts rotational evolution probabilistically.
- **ChronoFlow** incorporates cluster membership probabilities per star, and is **robust against observational selection effects in color and age**.
- With **ChronoFlow**, we can estimate stellar ages to a statistical uncertainty of **0.7 dex**, and cluster ages to **0.06 dex**.
- We have analyzed sources of possible systematic error, which in total add **0.06 dex** of uncertainty to inferred population ages. This results in a total error budget of **0.08 dex**.

**ChronoFlow** can be broadly applied as an age inference tool with confidence in the consideration of systematic uncertainties. It also represents a baseline that can now

be used to probe and compare theoretical models, providing insight into the physics that drive stellar spin down.

## 9. ACKNOWLEDGMENTS

P.R.V. was supported by funding from the Dunlap Institute, a Queen Elizabeth II Graduate Scholarship in Science and Technology from the Government of Ontario, and a Canada Graduate Scholarships – Master’s (CGS-M) Award and Postgraduate Scholarships - Doctoral (PGS-D) Award from the Natural Sciences and Engineering Research Council of Canada (NSERC). J.S.S. was supported by funding from the Dunlap Institute, an NSERC Banting Postdoctoral Fellowship, NSERC Discovery Grant RGPIN-2023-04849, and a University of Toronto Connaught New Researcher Award. This work was supported in part by a NSERC Discovery Grant (RGPIN-2020-04554) to G.M.E.

The authors would like to thank Diego Godoy-Rivera for inspiration and helpful feedback on this work. The authors would also like to thank Cecilia Garraffo and Kristina Monsch for hosting P.R.V. and J.S.S. at CfA for valuable collaboration time, and their feedback and ideas for this project. The authors would like to thank Steffani Grondin for valuable feedback on this paper, and Ryan Cloutier, Jennifer van Saders, Dario Fritzewski, Jason Curtis, and David Charbonneau for useful comments and insights.

## REFERENCES

- Agüeros, M. A., Bowsher, E. C., Bochanski, J. J., et al. 2018, *ApJ*, 862, 33, doi: [10.3847/1538-4357/aac6ed](https://doi.org/10.3847/1538-4357/aac6ed)
- Andrews, J. J., Curtis, J. L., Chanamé, J., et al. 2022, *AJ*, 163, 275, doi: [10.3847/1538-3881/ac6952](https://doi.org/10.3847/1538-3881/ac6952)
- Angus, R., Aigrain, S., Foreman-Mackey, D., & McQuillan, A. 2015, *MNRAS*, 450, 1787, doi: [10.1093/mnras/stv423](https://doi.org/10.1093/mnras/stv423)
- Angus, R., Morton, T. D., Foreman-Mackey, D., et al. 2019, *AJ*, 158, 173, doi: [10.3847/1538-3881/ab3c53](https://doi.org/10.3847/1538-3881/ab3c53)
- Balaguer-Núñez, L., Jordi, C., & Galadí-Enríquez, D. 2005, *A&A*, 437, 457, doi: [10.1051/0004-6361:20041792](https://doi.org/10.1051/0004-6361:20041792)
- Barnes, S. A. 2003, *ApJ*, 586, 464, doi: [10.1086/367639](https://doi.org/10.1086/367639)
- . 2007, *ApJ*, 669, 1167, doi: [10.1086/519295](https://doi.org/10.1086/519295)
- . 2010, *ApJ*, 722, 222, doi: [10.1088/0004-637X/722/1/222](https://doi.org/10.1088/0004-637X/722/1/222)
- Barnes, S. A., & Kim, Y.-C. 2010, *ApJ*, 721, 675, doi: [10.1088/0004-637X/721/1/675](https://doi.org/10.1088/0004-637X/721/1/675)
- Barnes, S. A., Weingrill, J., Fritzewski, D., Strassmeier, K. G., & Platais, I. 2016, *ApJ*, 823, 16, doi: [10.3847/0004-637X/823/1/16](https://doi.org/10.3847/0004-637X/823/1/16)
- Barnes, S. A., Weingrill, J., Granzer, T., Spada, F., & Strassmeier, K. G. 2015, *A&A*, 583, A73, doi: [10.1051/0004-6361/201526129](https://doi.org/10.1051/0004-6361/201526129)
- Beck, P. G., do Nascimento, J. D., J., Duarte, T., et al. 2017, *A&A*, 602, A63, doi: [10.1051/0004-6361/201629820](https://doi.org/10.1051/0004-6361/201629820)
- Beyer, A. C., & White, R. J. 2024, *ApJ*, 973, 28, doi: [10.3847/1538-4357/ad6b0d](https://doi.org/10.3847/1538-4357/ad6b0d)
- Borucki, W. J., Koch, D., Basri, G., et al. 2010, *Science*, 327, 977, doi: [10.1126/science.1185402](https://doi.org/10.1126/science.1185402)
- Bossini, D., Vallenari, A., Bragaglia, A., et al. 2019, *A&A*, 623, A108, doi: [10.1051/0004-6361/201834693](https://doi.org/10.1051/0004-6361/201834693)
- Bouma, L. G., Palumbo, E. K., & Hillenbrand, L. A. 2023, *ApJL*, 947, L3, doi: [10.3847/2041-8213/acc589](https://doi.org/10.3847/2041-8213/acc589)
- Boyle, A. W., & Bouma, L. G. 2022, arXiv e-prints, arXiv:2211.09822, doi: [10.48550/arXiv.2211.09822](https://doi.org/10.48550/arXiv.2211.09822)
- Cantat-Gaudin, T., Anders, F., Castro-Ginard, A., et al. 2020, *A&A*, 640, A1, doi: [10.1051/0004-6361/202038192](https://doi.org/10.1051/0004-6361/202038192)
- Cardelli, J. A., Clayton, G. C., & Mathis, J. S. 1989, *ApJ*, 345, 245, doi: [10.1086/167900](https://doi.org/10.1086/167900)

- Chiti, F., van Saders, J. L., Heintz, T. M., et al. 2024, arXiv e-prints, arXiv:2403.12129, doi: [10.48550/arXiv.2403.12129](https://doi.org/10.48550/arXiv.2403.12129)
- Cole-Kodikara, E. M., Barnes, S. A., Weingrill, J., & Granzer, T. 2023, *A&A*, 673, A119, doi: [10.1051/0004-6361/202245441](https://doi.org/10.1051/0004-6361/202245441)
- Cunha, M. S., Aerts, C., Christensen-Dalsgaard, J., et al. 2007, *A&A Rv*, 14, 217, doi: [10.1007/s00159-007-0007-0](https://doi.org/10.1007/s00159-007-0007-0)
- Currie, T., Hernandez, J., Irwin, J., et al. 2010, *ApJS*, 186, 191, doi: [10.1088/0067-0049/186/2/191](https://doi.org/10.1088/0067-0049/186/2/191)
- Curtis, J. L., Agüeros, M. A., Douglas, S. T., & Meibom, S. 2019, *ApJ*, 879, 49, doi: [10.3847/1538-4357/ab2393](https://doi.org/10.3847/1538-4357/ab2393)
- Curtis, J. L., Agüeros, M. A., Matt, S. P., et al. 2020, *ApJ*, 904, 140, doi: [10.3847/1538-4357/ab5f58](https://doi.org/10.3847/1538-4357/ab5f58)
- Deliyannis, C. P., Anthony-Twarog, B. J., Lee-Brown, D. B., & Twarog, B. A. 2019, *AJ*, 158, 163, doi: [10.3847/1538-3881/ab3fad](https://doi.org/10.3847/1538-3881/ab3fad)
- Delorme, P., Collier Cameron, A., Hebb, L., et al. 2011, *MNRAS*, 413, 2218, doi: [10.1111/j.1365-2966.2011.18299.x](https://doi.org/10.1111/j.1365-2966.2011.18299.x)
- Demarque, P., & Larson, R. 1964, *ApJ*, 140, 544, doi: [10.1086/147948](https://doi.org/10.1086/147948)
- Dotter, A. 2016, *ApJS*, 222, 8, doi: [10.3847/0067-0049/222/1/8](https://doi.org/10.3847/0067-0049/222/1/8)
- Douglas, S. T., Agüeros, M. A., Covey, K. R., et al. 2016, *ApJ*, 822, 47, doi: [10.3847/0004-637X/822/1/47](https://doi.org/10.3847/0004-637X/822/1/47)
- Douglas, S. T., Cargile, P. A., Matt, S. P., et al. 2024, *ApJ*, 962, 16, doi: [10.3847/1538-4357/ad0fe3](https://doi.org/10.3847/1538-4357/ad0fe3)
- Douglas, S. T., Curtis, J. L., Agüeros, M. A., et al. 2019, *ApJ*, 879, 100, doi: [10.3847/1538-4357/ab2468](https://doi.org/10.3847/1538-4357/ab2468)
- Dungee, R., van Saders, J., Gaidos, E., et al. 2022, *ApJ*, 938, 118, doi: [10.3847/1538-4357/ac90be](https://doi.org/10.3847/1538-4357/ac90be)
- Durkan, C., Bekasov, A., Murray, I., & Papamakarios, G. 2019, *Neural Spline Flows*. <https://arxiv.org/abs/1906.04032>
- Edenhofer, G., Zucker, C., Frank, P., et al. 2023, arXiv e-prints, arXiv:2308.01295, doi: [10.48550/arXiv.2308.01295](https://doi.org/10.48550/arXiv.2308.01295)
- El-Badry, K. 2024, *NewAR*, 98, 101694, doi: [10.1016/j.newar.2024.101694](https://doi.org/10.1016/j.newar.2024.101694)
- Foreman-Mackey, D., Hogg, D. W., Lang, D., & Goodman, J. 2013, *PASP*, 125, 306, doi: [10.1086/670067](https://doi.org/10.1086/670067)
- Fritzewski, D. J., Barnes, S. A., James, D. J., et al. 2019, *A&A*, 622, A110, doi: [10.1051/0004-6361/201833587](https://doi.org/10.1051/0004-6361/201833587)
- Fritzewski, D. J., Barnes, S. A., James, D. J., Järvinen, S. P., & Strassmeier, K. G. 2021, *A&A*, 656, A103, doi: [10.1051/0004-6361/202140896](https://doi.org/10.1051/0004-6361/202140896)
- Fritzewski, D. J., Barnes, S. A., Weingrill, J., et al. 2023, *A&A*, 674, A152, doi: [10.1051/0004-6361/202346083](https://doi.org/10.1051/0004-6361/202346083)
- Gaia Collaboration, Babusiaux, C., van Leeuwen, F., et al. 2018, *A&A*, 616, A10, doi: [10.1051/0004-6361/201832843](https://doi.org/10.1051/0004-6361/201832843)
- Gaia Collaboration, Vallenari, A., Brown, A. G. A., et al. 2023, *A&A*, 674, A1, doi: [10.1051/0004-6361/202243940](https://doi.org/10.1051/0004-6361/202243940)
- Galindo-Guil, F. J., Barrado, D., Bouy, H., et al. 2022, *A&A*, 664, A70, doi: [10.1051/0004-6361/202141114](https://doi.org/10.1051/0004-6361/202141114)
- Garraffo, C., Drake, J. J., Dotter, A., et al. 2018, *ApJ*, 862, 90, doi: [10.3847/1538-4357/aace5d](https://doi.org/10.3847/1538-4357/aace5d)
- Geller, A. M., Latham, D. W., & Mathieu, R. D. 2015, *AJ*, 150, 97, doi: [10.1088/0004-6256/150/3/97](https://doi.org/10.1088/0004-6256/150/3/97)
- Godoy-Rivera, D., Pinsonneault, M. H., & Rebull, L. M. 2021, *ApJS*, 257, 46, doi: [10.3847/1538-4365/ac2058](https://doi.org/10.3847/1538-4365/ac2058)
- Gossage, S., Dotter, A., Garraffo, C., et al. 2021, *ApJ*, 912, 65, doi: [10.3847/1538-4357/abebdf](https://doi.org/10.3847/1538-4357/abebdf)
- Gossage, S., Kiman, R., Monsch, K., et al. 2024, arXiv e-prints, arXiv:2410.20000, doi: [10.48550/arXiv.2410.20000](https://doi.org/10.48550/arXiv.2410.20000)
- Green, G. 2018, *The Journal of Open Source Software*, 3, 695, doi: [10.21105/joss.00695](https://doi.org/10.21105/joss.00695)
- Green, G. M., Schlafly, E., Zucker, C., Speagle, J. S., & Finkbeiner, D. 2019, *ApJ*, 887, 93, doi: [10.3847/1538-4357/ab5362](https://doi.org/10.3847/1538-4357/ab5362)
- Grondin, S. M., Drout, M. R., Nordhaus, J., et al. 2024, *ApJ*, 976, 102, doi: [10.3847/1538-4357/ad7500](https://doi.org/10.3847/1538-4357/ad7500)
- Gutiérrez Albarrán, M. L., Montes, D., Gómez Garrido, M., et al. 2020, *A&A*, 643, A71, doi: [10.1051/0004-6361/202037620](https://doi.org/10.1051/0004-6361/202037620)
- Hall, O. J., Davies, G. R., van Saders, J., et al. 2021, *Nature Astronomy*, 5, 707, doi: [10.1038/s41550-021-01335-x](https://doi.org/10.1038/s41550-021-01335-x)
- Hartman, J. D., Bakos, G. Á., Kovács, G., & Noyes, R. W. 2010, *MNRAS*, 408, 475, doi: [10.1111/j.1365-2966.2010.17147.x](https://doi.org/10.1111/j.1365-2966.2010.17147.x)
- Hartman, J. D., Bakos, G. Á., Noyes, R. W., et al. 2011, *AJ*, 141, 166, doi: [10.1088/0004-6256/141/5/166](https://doi.org/10.1088/0004-6256/141/5/166)
- Hartman, J. D., Gaudi, B. S., Pinsonneault, M. H., et al. 2009, *ApJ*, 691, 342, doi: [10.1088/0004-637X/691/1/342](https://doi.org/10.1088/0004-637X/691/1/342)
- Howell, S. B., Sobek, C., Haas, M., et al. 2014, *PASP*, 126, 398, doi: [10.1086/676406](https://doi.org/10.1086/676406)
- Irwin, J., Aigrain, S., Bouvier, J., et al. 2009, *MNRAS*, 392, 1456, doi: [10.1111/j.1365-2966.2008.14158.x](https://doi.org/10.1111/j.1365-2966.2008.14158.x)
- Irwin, J., Hodgkin, S., Aigrain, S., et al. 2008, *MNRAS*, 383, 1588, doi: [10.1111/j.1365-2966.2007.12669.x](https://doi.org/10.1111/j.1365-2966.2007.12669.x)
- . 2007, *MNRAS*, 377, 741, doi: [10.1111/j.1365-2966.2007.11640.x](https://doi.org/10.1111/j.1365-2966.2007.11640.x)
- Jeffries, R. D. 2014, in *EAS Publications Series*, Vol. 65, *EAS Publications Series*, ed. Y. Lebreton, D. Valls-Gabaud, & C. Charbonnel, 289–325, doi: [10.1051/eas/1465008](https://doi.org/10.1051/eas/1465008)
- Jeffries, R. D., Jackson, R. J., & Binks, A. S. 2023a, *MNRAS*, 526, 1260, doi: [10.1093/mnras/stad2845](https://doi.org/10.1093/mnras/stad2845)

- Jeffries, R. D., Jackson, R. J., Sun, Q., & Deliyannis, C. P. 2021, *MNRAS*, 500, 1158, doi: [10.1093/mnras/staa3141](https://doi.org/10.1093/mnras/staa3141)
- Jeffries, R. D., & Oliveira, J. M. 2005, *MNRAS*, 358, 13, doi: [10.1111/j.1365-2966.2005.08820.x](https://doi.org/10.1111/j.1365-2966.2005.08820.x)
- Jeffries, R. D., Jackson, R. J., Wright, N. J., et al. 2023b, *MNRAS*, 523, 802, doi: [10.1093/mnras/stad1293](https://doi.org/10.1093/mnras/stad1293)
- Kounkel, M., & Covey, K. 2019, *AJ*, 158, 122, doi: [10.3847/1538-3881/ab339a](https://doi.org/10.3847/1538-3881/ab339a)
- Kraft, R. P. 1967, *ApJ*, 150, 551, doi: [10.1086/149359](https://doi.org/10.1086/149359)
- Krolikowski, D. M., Kraus, A. L., & Rizzuto, A. C. 2021, *AJ*, 162, 110, doi: [10.3847/1538-3881/ac0632](https://doi.org/10.3847/1538-3881/ac0632)
- Libralato, M., Bedin, L. R., Nardiello, D., & Piotto, G. 2016, *MNRAS*, 456, 1137, doi: [10.1093/mnras/stv2628](https://doi.org/10.1093/mnras/stv2628)
- Lindgren, L., Bastian, U., Biermann, M., et al. 2021, *A&A*, 649, A4, doi: [10.1051/0004-6361/202039653](https://doi.org/10.1051/0004-6361/202039653)
- Long, L., Bi, S., Zhang, J., et al. 2023, *ApJS*, 268, 30, doi: [10.3847/1538-4365/ace5af](https://doi.org/10.3847/1538-4365/ace5af)
- Loshchilov, I., & Hutter, F. 2017, *SGDR: Stochastic Gradient Descent with Warm Restarts*. <https://arxiv.org/abs/1608.03983>
- Lu, Y., Angus, R., Foreman-Mackey, D., & Hattori, S. 2024a, *AJ*, 167, 159, doi: [10.3847/1538-3881/ad28b9](https://doi.org/10.3847/1538-3881/ad28b9)
- Lu, Y. L., See, V., Amard, L., Angus, R., & Matt, S. P. 2024b, *Nature Astronomy*, 8, 223, doi: [10.1038/s41550-023-02126-2](https://doi.org/10.1038/s41550-023-02126-2)
- McInnes, L., Healy, J., & Astels, S. 2017, *The Journal of Open Source Software*, 2, doi: [10.21105/joss.00205](https://doi.org/10.21105/joss.00205)
- Meibom, S., Barnes, S. A., Platais, I., et al. 2015, *Nature*, 517, 589, doi: [10.1038/nature14118](https://doi.org/10.1038/nature14118)
- Meibom, S., Mathieu, R. D., & Stassun, K. G. 2009, *ApJ*, 695, 679, doi: [10.1088/0004-637X/695/1/679](https://doi.org/10.1088/0004-637X/695/1/679)
- Meibom, S., Mathieu, R. D., Stassun, K. G., Liebesny, P., & Saar, S. H. 2011, *ApJ*, 733, 115, doi: [10.1088/0004-637X/733/2/115](https://doi.org/10.1088/0004-637X/733/2/115)
- Messina, S. 2001, *A&A*, 371, 1024, doi: [10.1051/0004-6361:20010466](https://doi.org/10.1051/0004-6361:20010466)
- Metcalf, T. S., Finley, A. J., Kochukhov, O., et al. 2022, *ApJL*, 933, L17, doi: [10.3847/2041-8213/ac794d](https://doi.org/10.3847/2041-8213/ac794d)
- Moraux, E., Artemenko, S., Bouvier, J., et al. 2013, *A&A*, 560, A13, doi: [10.1051/0004-6361/201321508](https://doi.org/10.1051/0004-6361/201321508)
- Nardiello, D., Bedin, L. R., Nascimbeni, V., et al. 2015, *MNRAS*, 447, 3536, doi: [10.1093/mnras/stu2697](https://doi.org/10.1093/mnras/stu2697)
- Oliveira, J. M., Jeffries, R. D., Devey, C. R., et al. 2003, *MNRAS*, 342, 651, doi: [10.1046/j.1365-8711.2003.06592.x](https://doi.org/10.1046/j.1365-8711.2003.06592.x)
- Pass, E. K., Charbonneau, D., Irwin, J. M., & Winters, J. G. 2022, *ApJ*, 936, 109, doi: [10.3847/1538-4357/ac7da8](https://doi.org/10.3847/1538-4357/ac7da8)
- Penoyre, Z., Belokurov, V., & Evans, N. W. 2022, *MNRAS*, 513, 5270, doi: [10.1093/mnras/stac1147](https://doi.org/10.1093/mnras/stac1147)
- Popinchalk, M., Faherty, J. K., Kiman, R., et al. 2021, *ApJ*, 916, 77, doi: [10.3847/1538-4357/ac0444](https://doi.org/10.3847/1538-4357/ac0444)
- Prosser, C. F., Shetrone, M. D., Marilli, E., et al. 1993, *PASP*, 105, 1407, doi: [10.1086/133322](https://doi.org/10.1086/133322)
- Prosser, C. F., Shetrone, M. D., Dasgupta, A., et al. 1995, *PASP*, 107, 211, doi: [10.1086/133541](https://doi.org/10.1086/133541)
- Radick, R. R., Lockwood, G. W., Skiff, B. A., & Thompson, D. T. 1995, *ApJ*, 452, 332, doi: [10.1086/176305](https://doi.org/10.1086/176305)
- Radick, R. R., Thompson, D. T., Lockwood, G. W., Duncan, D. K., & Baggett, W. E. 1987, *ApJ*, 321, 459, doi: [10.1086/165645](https://doi.org/10.1086/165645)
- Rampalli, R., Agüeros, M. A., Curtis, J. L., et al. 2021, *ApJ*, 921, 167, doi: [10.3847/1538-4357/ac0c1e](https://doi.org/10.3847/1538-4357/ac0c1e)
- Ratzenböck, S., Großschedl, J. E., Möller, T., et al. 2023, *A&A*, 677, A59, doi: [10.1051/0004-6361/202243690](https://doi.org/10.1051/0004-6361/202243690)
- Rebull, L. M., Stauffer, J. R., Cody, A. M., et al. 2018, *AJ*, 155, 196, doi: [10.3847/1538-3881/aab605](https://doi.org/10.3847/1538-3881/aab605)
- Rebull, L. M., Stauffer, J. R., Hillenbrand, L. A., et al. 2017, *ApJ*, 839, 92, doi: [10.3847/1538-4357/aa6aa4](https://doi.org/10.3847/1538-4357/aa6aa4)
- Rebull, L. M., Stauffer, J. R., Bouvier, J., et al. 2016, *AJ*, 152, 113, doi: [10.3847/0004-6256/152/5/113](https://doi.org/10.3847/0004-6256/152/5/113)
- Ricker, G. R., Winn, J. N., Vanderspek, R., et al. 2015, *Journal of Astronomical Telescopes, Instruments, and Systems*, 1, 014003, doi: [10.1117/1.JATIS.1.1.014003](https://doi.org/10.1117/1.JATIS.1.1.014003)
- Riello, M., De Angeli, F., Evans, D. W., et al. 2021, *A&A*, 649, A3, doi: [10.1051/0004-6361/202039587](https://doi.org/10.1051/0004-6361/202039587)
- Santos, A. R. G., Breton, S. N., Mathur, S., & García, R. A. 2021, *ApJS*, 255, 17, doi: [10.3847/1538-4365/ac033f](https://doi.org/10.3847/1538-4365/ac033f)
- Santos, A. R. G., García, R. A., Mathur, S., et al. 2019, *ApJS*, 244, 21, doi: [10.3847/1538-4365/ab3b56](https://doi.org/10.3847/1538-4365/ab3b56)
- Schatzman, E. 1962, *Annales d'Astrophysique*, 25, 18
- Schlafly, E. F., & Finkbeiner, D. P. 2011, *ApJ*, 737, 103, doi: [10.1088/0004-637X/737/2/103](https://doi.org/10.1088/0004-637X/737/2/103)
- Schlegel, D. J., Finkbeiner, D. P., & Davis, M. 1998, *ApJ*, 500, 525, doi: [10.1086/305772](https://doi.org/10.1086/305772)
- Silva Aguirre, V., Lund, M. N., Antia, H. M., et al. 2017, *ApJ*, 835, 173, doi: [10.3847/1538-4357/835/2/173](https://doi.org/10.3847/1538-4357/835/2/173)
- Silva-Beyer, J., Godoy-Rivera, D., & Chanamé, J. 2022, *arXiv e-prints*, arXiv:2210.01137. <https://arxiv.org/abs/2210.01137>
- Skumanich, A. 1972, *ApJ*, 171, 565, doi: [10.1086/151310](https://doi.org/10.1086/151310)
- Soares-Furtado, M., Hartman, J. D., Bhatti, W., et al. 2020, *ApJS*, 246, 15, doi: [10.3847/1538-4365/ab5fcf](https://doi.org/10.3847/1538-4365/ab5fcf)
- Soderblom, D. R. 2010, *ARA&A*, 48, 581, doi: [10.1146/annurev-astro-081309-130806](https://doi.org/10.1146/annurev-astro-081309-130806)
- Spada, F., & Lanzafame, A. C. 2020, *A&A*, 636, A76, doi: [10.1051/0004-6361/201936384](https://doi.org/10.1051/0004-6361/201936384)
- Stauffer, J. R., Schultz, G., & Kirkpatrick, J. D. 1998, *ApJL*, 499, L199, doi: [10.1086/311379](https://doi.org/10.1086/311379)
- Stauffer, J. R., Barrado y Navascués, D., Bouvier, J., et al. 1999, *ApJ*, 527, 219, doi: [10.1086/308069](https://doi.org/10.1086/308069)

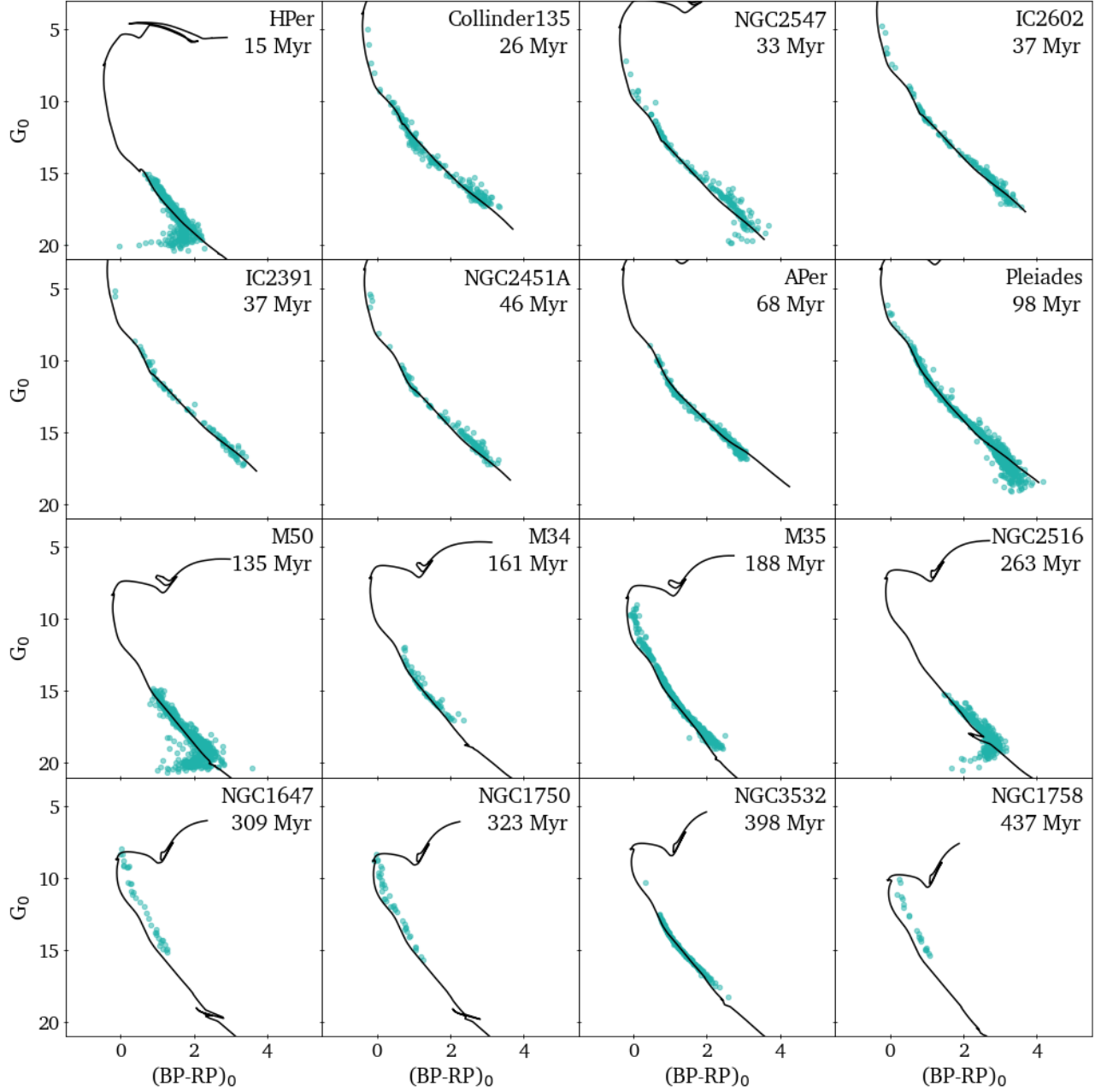
- Taylor, M. B. 2005, in *Astronomical Society of the Pacific Conference Series*, Vol. 347, *Astronomical Data Analysis Software and Systems XIV*, ed. P. Shopbell, M. Britton, & R. Ebert, 29
- Van-Lane, P., Speagle, J. S., & Douglas, S. 2023, A Novel Application of Conditional Normalizing Flows: Stellar Age Inference with Gyrochronology.  
<https://arxiv.org/abs/2307.08753>
- van Leeuwen, F., de Bruijne, J. H. J., Arenou, F., et al. 2018, Gaia DR2 documentation, Gaia DR2 documentation, European Space Agency; Gaia Data Processing and Analysis Consortium. Online at <https://gea.esac.esa.int/archive/documentation/GDR2/>
- van Saders, J. L., Ceillier, T., Metcalfe, T. S., et al. 2016, *Nature*, 529, 181, doi: [10.1038/nature16168](https://doi.org/10.1038/nature16168)
- Wang, S., & Chen, X. 2019, *ApJ*, 877, 116, doi: [10.3847/1538-4357/ab1c61](https://doi.org/10.3847/1538-4357/ab1c61)
- Weber, E. J., & Davis, Leverett, J. 1967, *ApJ*, 148, 217, doi: [10.1086/149138](https://doi.org/10.1086/149138)
- Wilson, O. C. 1966, *ApJ*, 144, 695, doi: [10.1086/148649](https://doi.org/10.1086/148649)
- Zhang, X., Green, G. M., & Rix, H.-W. 2023, *MNRAS*, 524, 1855, doi: [10.1093/mnras/stad1941](https://doi.org/10.1093/mnras/stad1941)



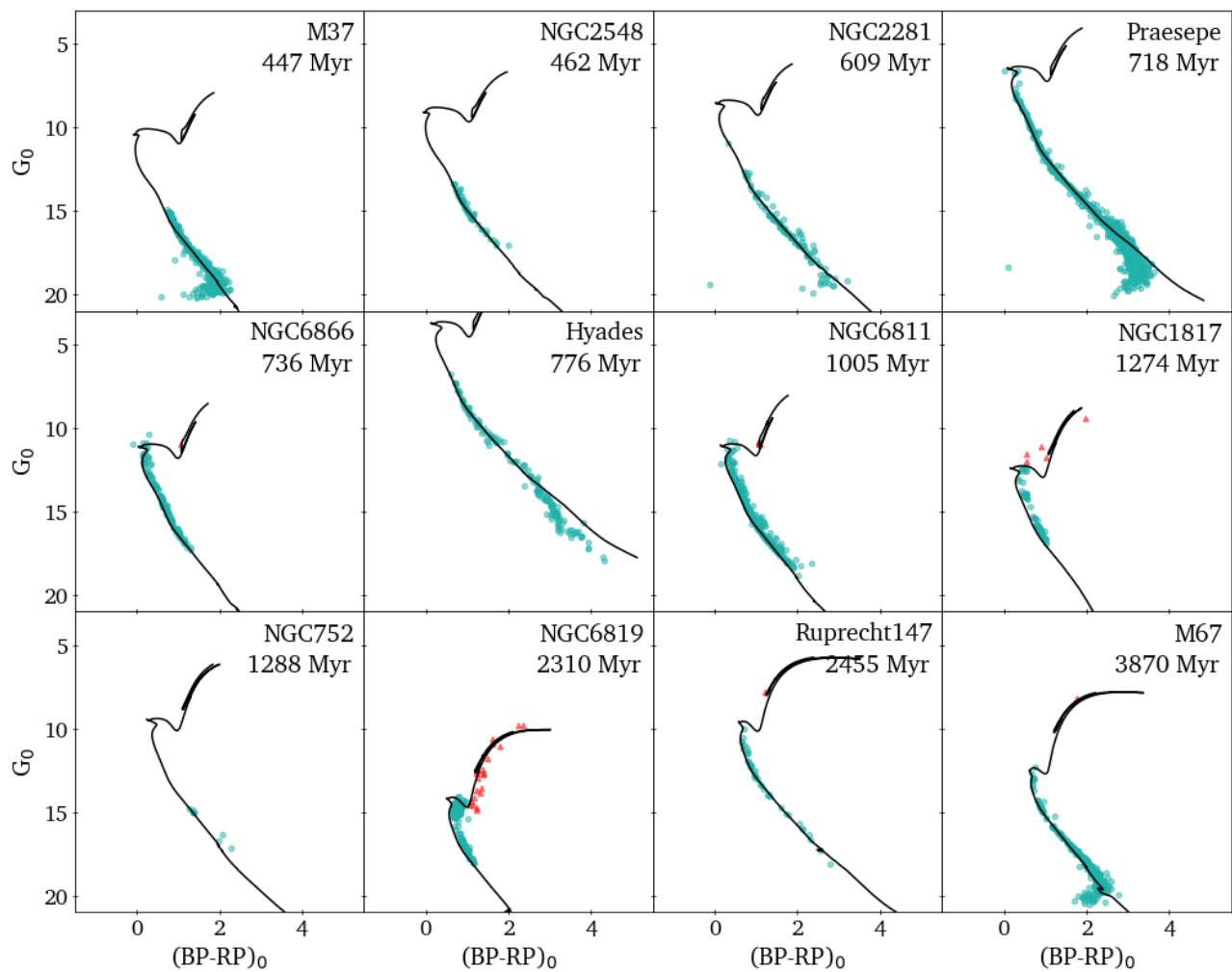
APPENDIX

A. CLUSTER CMDS AND PROPER MOTION PLOTS

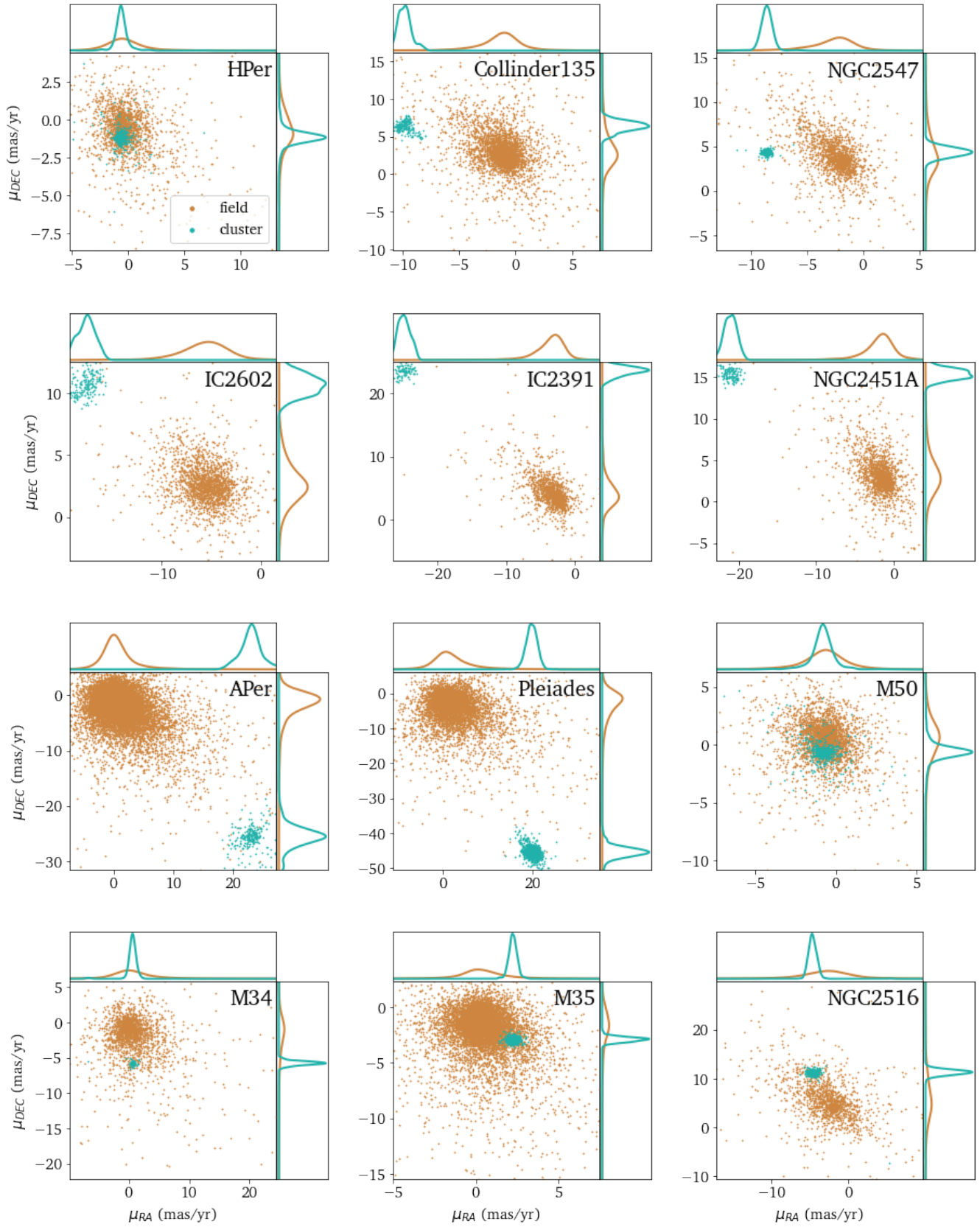
Figure 19 presents CMDs for each cluster, comparing observations to the theoretical isochrones generated using **brutus**<sup>7</sup> (which implements MIST isochrones; Dotter 2016) at the fiducial literature age for each cluster. The red triangles indicate the stars we exclude from our catalog due to the final CMD cut. Figure 20 shows the distributions in proper motion of catalog stars compared to field stars around each cluster.

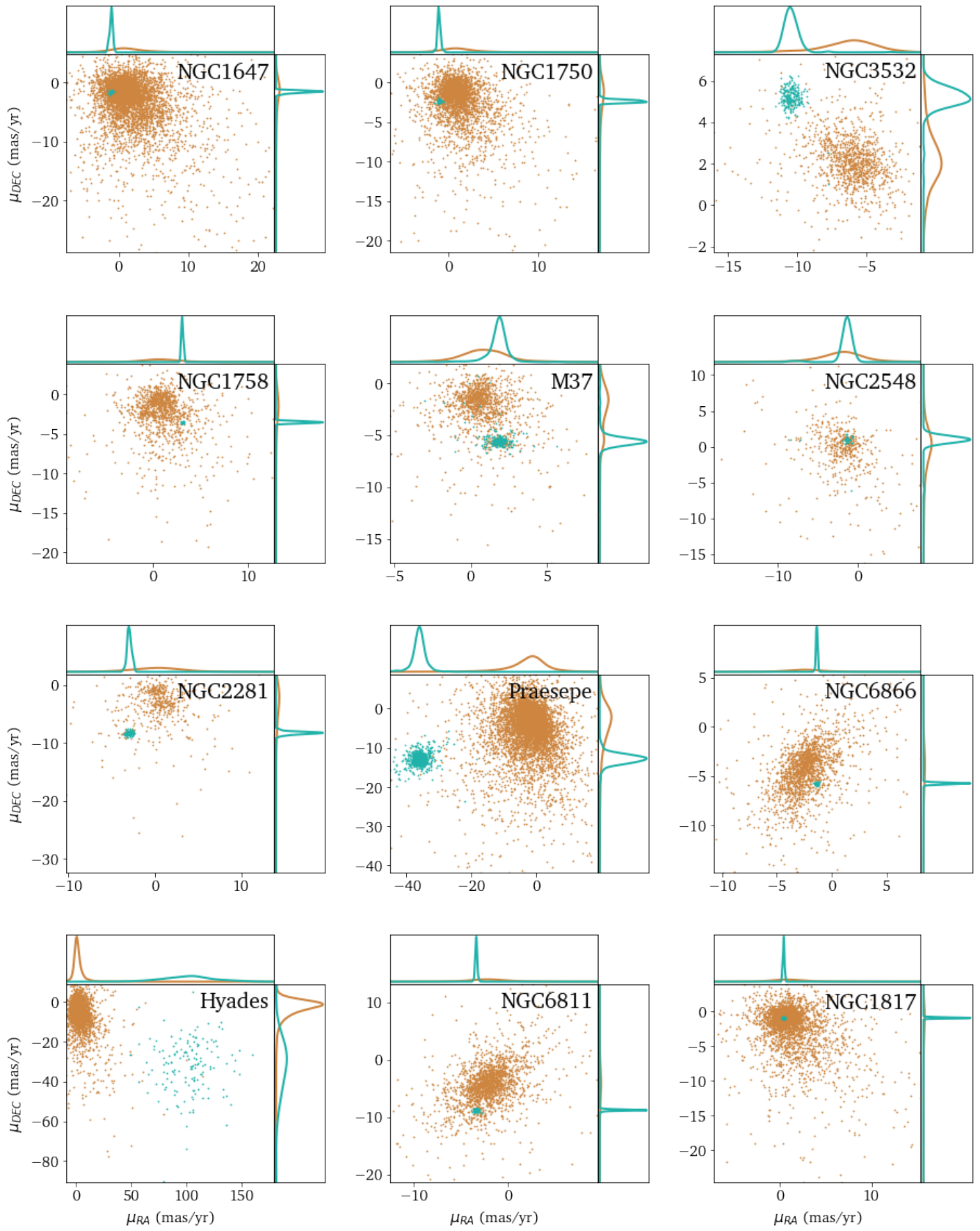


<sup>7</sup> <https://github.com/joshspeagle/brutus/tree/master>



**Figure 19.** Cluster CMDs in increasing order of cluster age (excluding the Taurus and Sco-Cen regions). Both the  $G_0$  magnitudes and  $(BP - RP)_0$  colours are de-reddened using the extinctions from [Edenhofer et al. \(2023\)](#). Isochrones are generated using the fiducial cluster ages from literature; they are not estimates inferred by our model. Red triangles are stars that we have excluded from our catalog due to their location on the CMDs.





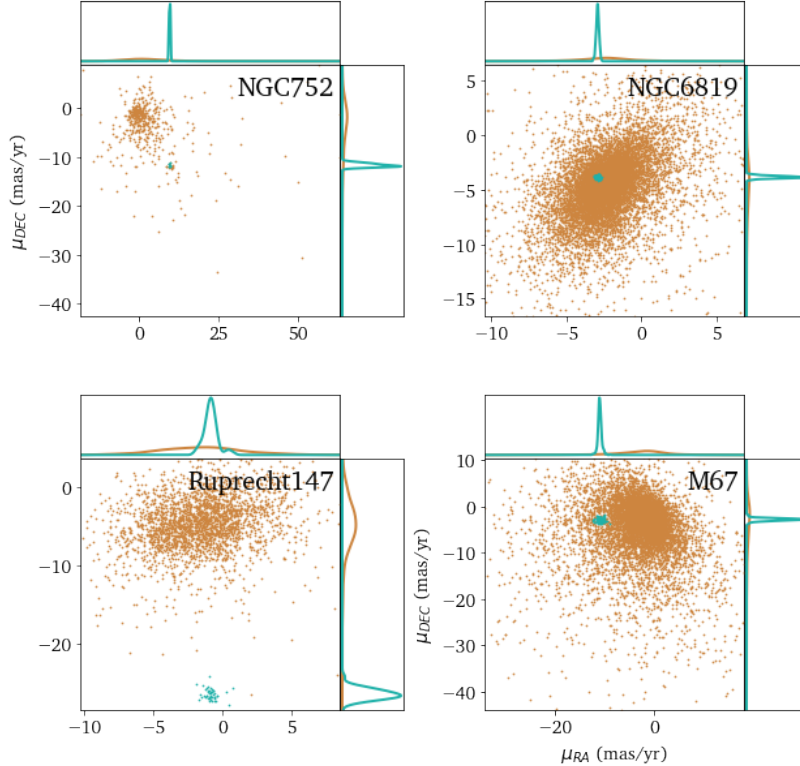


**Figure 20.** Proper motion distributions for each cluster. Cluster members are plotted against a 2000-star sample drawn randomly from between  $4\sigma$  and  $10\sigma$  in distance from the cluster center. Marginal distributions for  $\mu_{RA}$  and  $\mu_{DEC}$  are plotted along the axes for both cluster members (teal) and field stars (brown).

## B. CUTS APPLIED TO LITERATURE ROTATION CATALOGS

Here we summarize quality cuts we made when compiling our catalog, based only on the information provided by the literature sources. Many of these are designed to eliminate binaries.

- [Curtis et al. \(2020\)](#) already applied quality cuts when compiling their rotators, so we use that catalog (Table 5 in that work) with no additional filters for **NGC 752**, **NGC 6811**, **NGC 6819**, **Pleiades**, and **Ruprecht 147**. We do not use the Praesepe data from this catalog, and instead use [Rampalli et al. \(2021\)](#), which is a revised catalog built on the [Curtis et al. \(2020\)](#) data.
- We do not apply any additional cuts to the [Barnes et al. \(2015\)](#) **NGC 2548** catalog (Table 2 in that work).
- We do not apply additional cuts to the [Fritzewski et al. \(2023\)](#) **NGC 2281** catalog (Table 2 in that work).
- We exclude stars in the [Douglas et al. \(2019\)](#) **Hyades** catalog (Tables 2/3 of that work) having a `Conf` flag of `Y` (ie. confirmed binaries).
- We exclude all rotators from the [Godoy-Rivera et al. \(2021\)](#) catalog (Table F1 of that paper) that were assigned the classification of `non-member`.
- We only include rotators from the [Douglas et al. \(2024\)](#) catalog (Table 4 of that work) that have a `to_plot` value of 1; this was used as a membership cut in that work.
- We apply several cuts to the [Long et al. \(2023\)](#) catalog (Table 5 of that work):
  1. We only include stars with `BinPhot` and `BinSpec` values that are both 0 (ie. photometrically and spectroscopically single stars).

2. We only include stars with a `BinRUWE` value of 0. This corresponds to stars with a Gaia `RUWE` value of  $\leq 1.4$ , which is a cut we apply in our final selection anyways.
  3. We only include stars with a `BinFlag` value of 0 or 1 (either a MS single star or unknown).
  4. We also exclude four Pleiades stars that L23 sourced directly from the [Hartman et al. \(2010\)](#) catalog, but for which the original rotation period was measured in other works ([Prosser et al. 1993](#); a reference labelled P95 which we assume to be [Prosser et al. 1995](#); and [Messina 2001](#)), and for which [Hartman et al. \(2010\)](#) were not able to measure rotation periods themselves.
- We only include rotators from [Boyle & Bouma \(2022\)](#) (Table 3 in that work) where the `in_gyro_sample` flag is set to `True`. These are the subset of stars that the authors use to calibrate their model.
  - We only keep stars from [Moraux et al. \(2013\)](#) (Table 2 in that work) with a `bin` flag of 1. This corresponds to photometrically single stars.
  - We only keep stars from [Meibom et al. \(2011\)](#) (Table 2 in that work) that are kinematic and/or photometric members: i.e. having a `mcode` value of KM or PM.
  - We only include stars with a `single` flag of `True` and a `binary` flag of `False` from [Dungee et al. \(2022\)](#) (Table 2 in that work). We also exclude stars with a false-alarm probability (FAP) of  $i=1\%$ , which the authors use as the upper limit for which periodic signals are considered significant. We exclude stars with a measured period of  $i=175$  days, following the authors' requirement that stars have at least five completed periods within the light-curve duration to be considered reliable.
  - We only include stars from [Barnes et al. \(2016\)](#) (Table 1 in that work) having a `Member` flag of SM (i.e. single members).
  - We only include stars from [Rebull et al. \(2018\)](#) (Table 1 of that work) having a `Rdist` flag of `no`, meaning that there were not resolved distant peaks in the periodogram, which the authors would interpret as a binary. Although resolved close peaks could also be indicative of binaries, they could result from differential surface rotation, so we do not apply a cut based on the latter phenomenon.
  - We only include stars from [Rampalli et al. \(2021\)](#) (Table 3 of that work) having a `Bin` flag of 0 (i.e. non-binary stars) and a `QFClean` flag of 1. The latter cut restricts our sample to only stars with high-quality light curve flags.
  - We only include stars from [Fritzewski et al. \(2021\)](#) catalog (Table 2 of that work) having a `Binary` flag of 0.

### C. NOTES AND EDGE CASES FROM ROTATION PERIOD COMPILATION

Here we describe edge cases and duplication that we encountered when compiling our rotator catalog.

#### C.1. *Multiple catalog using the same source measurement*

Here is an extended description of the 421 rotation periods that were cited by multiple source catalogs (as described in §2):

- Both [Long et al. \(2023\)](#) and [Douglas et al. \(2019\)](#) used rotation periods measured by both [Delorme et al. \(2011\)](#) and [Hartman et al. \(2011\)](#) in their Hyades rotator catalogs.
- [Long et al. \(2023\)](#) cited M67 rotation periods directly from [Dungee et al. \(2022\)](#), however we consider these to be different catalogs since [Long et al. \(2023\)](#) calculated their own set of M67 rotation periods as well.
- Similarly, [Long et al. \(2023\)](#) cited Ruprecht 147 rotation periods directly from [Curtis et al. \(2020\)](#), along with measuring their own rotation periods.
- [Godoy-Rivera et al. \(2021\)](#) and [Curtis et al. \(2020\)](#) both cited NGC 6811 rotation periods directly from [Curtis et al. \(2019\)](#).
- [Godoy-Rivera et al. \(2021\)](#) and [Curtis et al. \(2020\)](#) both cited Pleiades rotation periods directly from [Rebull et al. \(2016\)](#).

### C.2. *Hyades*

Both the Douglas et al. (2019) and Long et al. (2023) catalogs use rotation periods measured by Hartman et al. (2011). Long et al. (2023) include one rotator and Douglas et al. (2019) include four, (of which one is the rotator used by Long et al. 2023). Both catalogs also share eight rotators measured by Delorme et al. (2011), of which two have a disagreement in reported period as cited in the catalogs. In both cases, the values reported by Douglas et al. (2019) match those reported directly by Delorme et al. (2011), so we use these values. Long et al. (2023) also include one rotator that is not part of the Douglas et al. (2019) catalog; Douglas et al. (2019) include 16 that are not part of the Long et al. (2023) catalog.

### C.3. *M35*

Long et al. (2023) reported rotation periods for M35 from a number of sources which overlap. In particular, they cite rotation periods directly from Meibom et al. (2009), Libralato et al. (2016), and Jeffries et al. (2021). Since Jeffries et al. (2021) themselves compiled their rotation periods from both Meibom et al. (2009) and Libralato et al. (2016), we checked for duplicates. We found none, so no further analysis was required.

#### C.3.1. *M67*

Long et al. (2023) used 10 stars with rotation periods measured by Dungee et al. (2022) that were not considered in the final Dungee et al. (2022) catalog. One of these has a measured rotation period but a FAP  $\geq 0.01$  (which was used as a quality cut by Dungee et al. 2022). The other nine stars do not actually have rotation periods reported by Dungee et al. (2022) catalog, so we were not able to determine where Long et al. (2023) obtained these values from. As such, we exclude these 10 stars from our final catalog. The other 45 rotation periods cited by Long et al. (2023) from Dungee et al. (2022) agree with the values presented by the latter.

### C.4. *NGC2516*

There appears to be duplication in the NGC 2516 data from Irwin et al. (2007) as compiled by Godoy-Rivera et al. (2021). Stars N2516-2-1-1441 and N2516-1-8-1419 are crossmatched to the same Gaia DR2 ID, and have similar rotation periods (1.461 and 1.465 days, respectively). We therefore remove the latter entry from our catalog. This also occurs with N2516-1-8-862 and N2516-2-1-843 (rotation periods of 1.545 and 1,546 respectively), so we removed the former from our catalog. We saw this again with N2516-1-8-1300 and N2516-2-1-1317 (both having a rotation period of 0.37 days), and removed the former. Finally, we saw this with N2516-1-8-2732 and N2516-2-1-2854 too (both having rotation periods of 0.341 days), and removed the former.

### C.5. *NGC6811*

Godoy-Rivera et al. (2021) include 34 rotators measured by Curtis et al. (2019), however 10 of their reported periods differ from the C19 values. In these cases we use the rotation periods directly from Curtis et al. (2019). Additionally, they include five rotators from the Santos et al. (2021, 2019) catalogs that were included in preliminary versions but not in the final published versions of those catalogs for various reasons. From private communication with Diego Godoy-Rivera, we determined that KIC 9656397 was a F-type eclipsing binary which should not be included in our sample, but the other four were reliable measurements which we kept.

### C.6. *Ruprecht 147*

The Long et al. (2023) catalog directly uses the rotation period measurements for 12 stars from Curtis et al. (2020). Out of these, we found seven matches in Curtis et al. (2020) catalog based on our crossmatch from Long et al. (2023) Gaia DR3 IDs to Curtis et al. (2020) Gaia DR2 IDs. For all seven, the rotation period is accurately reported. For the other five stars, no match was found in Curtis et al. (2020) catalog and none of the periods reported in Long et al. (2023) are close matches to periods in Curtis et al. (2020) catalog, so we exclude these rotation periods from our catalog.

## D. NOTES AND EDGE CASES FROM GAIA DR3 CROSSMATCH

Here we describe the steps we took to crossmatch all rotation periods to Gaia DR3:

1. If a star had a DR2 ID in the source catalog, we found the nearest neighbors in DR3 using the `gaiaedr3.dr2_neighbourhood` table. If there are multiple matches, we consider the angular and magnitude differences, and select the best match based on both criteria. We find a match for 2,495 rotators this way.

2. If the star had a DR2 ID but no neighbor in the above step, or did not have a Gaia DR2 ID in the source catalog, we used `topcat` (Taylor 2005) and/or the Gaia archive search to find the closest match within 1" using the R.A. and Decl. values provided with the catalog. In some cases this radius had to be extended to 2" to find a match.
3. There were 89 stars in the Godoy-Rivera et al. (2021) catalog for which no R.A. or Decl. was provided in that paper, but for which we found measurements in the rotation source catalogs for those rotators. 17 of these had Gaia DR3 matches within 1", however four of those 17 were ambiguous so we exclude those from our sample. The other 72 had matches within 10", however we only include the 25 of those which were unambiguous in our final catalog.
4. For H Persei, 483 of the 507 stars in the Moraux et al. (2013) catalog had Gaia DR3 crossmatches within 1as. An additional 6 had crossmatches within 5as, and 15 had crossmatches between 5 and 10as. At these larger radii, since the stars often had multiple crossmatches, we excluded these from our catalog and retain the 483 initial 1" crossmatches.
5. The crossmatches were all double checked using apparent magnitudes in the G and V bands where available (we converted G to V and vice versa where necessary using the  $G - V$  and  $B - V$  relationships presented in table 5.8 of van Leeuwen et al. 2018). In some cases, better matches were found based on a slightly larger angular difference but smaller difference in apparent magnitude. 15 stars were manually corrected to a different Gaia DR3 after this magnitude comparison.

There were 172 stars that corresponded to members of different clusters in different catalogs (but matched to the same Gaia DR3 ID). 169 of these were classified as Upper Scorpius by Rebull et al. (2018) catalog but  $\rho$  Ophiucus by Long et al. (2023). The rotation period measurements were very consistent for each. This is not an issue since we assigned all members of the Sco-Cen association to subgroups using the Ratzenböck et al. (2023) classifications anyway. In two other cases, one record was a direct match based on the Gaia DR3 ID, and one was a best fit match based on the DR2 ID. In these cases we kept the record with the matching DR3 ID. In the last case, the same DR3 ID was present in the source catalog for two different clusters. We excluded this star from all further analysis.

We also exclude two stars from our catalog which are members of Taurus subgroups according to Krolkowski et al. (2021), but are part of the Douglas et al. (2019) and Godoy-Rivera et al. (2021) Hyades and Pleiades catalogs respectively.

## E. CLUSTER MEMBERSHIP PROBABILITIES

Here we describe how we assigned cluster membership probabilities to rotators where no quantitative membership probability was provided in the data source catalog.

### E.1. Godoy Rivera et al. (2021): M37, M50, NGC 2516, NGC 2547, NGC 6811, Pleiades, Praesepe

The Godoy-Rivera et al. (2021) catalog contains cluster membership probabilities for each star, except those with insufficient Gaia DR2 data to be assigned a membership probability. These stars, designated as part of the *no-info* group by Godoy-Rivera et al. (2021), we assign a probability of 0.5 to.

### E.2. Douglas et al. (2024): Collinder 135, IC 2391, IC 2602, NGC 2451A, NGC 2547

For the Douglas et al. (2024) sources, we adopt the HDBScan membership probability provided for each star as the cluster membership probability. The exception to this is Gaia DR3 ID 5602911354490249344, which has no HDBScan membership probability provided or GES membership probability, but a Cantat-Gaudin et al. (2020) value of 1, which we adopt.

### E.3. Douglas et al. (2019): Hyades and Praesepe

Douglas et al. (2019) use a membership catalog compiled from several sources. Since no individual stellar cluster membership probabilities are provided there, we use a default value of 0.9. It is worth noting that some of these stars were not classified as cluster members according to Gaia Collaboration et al. (2018), however this may be due to Gaia quality cuts, and other good measurements are available.



E.4. *Rampalli et al. (2021): Praesepe*

Rampalli et al. (2021) also compile a membership catalog from multiple sources, and define all as having a 70% cluster membership probability. Naively assuming a uniform distribution in probability space, we assign a value of 0.85 for all of these stars.

E.5. *NGC 3532*

For NGC 3532, we use the radial velocity probabilities as calculated by Fritzewski et al. (2019) as our cluster membership probabilities. Where these are not available (this is the case for 9 of the 139 stars), we adopt a probability of 0.9.

E.6. *NGC 2281*

No quantitative membership probabilities were provided by Fritzewski et al. (2023) for NGC 2281, however they considered photometry, astrometry and radial velocities in their expansion of the NGC 2281 catalog from Kounkel & Covey (2019), which also did not provide quantitative membership probabilities. We adopt 0.9 as the default value for this cluster.

E.7. *Barnes et al. (2016): M67*

Barnes et al. (2016) use the M67 membership catalog from Geller et al. (2015), which computes radial velocity cluster membership values, and compares proper motion cluster membership probabilities from four literature sources. We take the average value across the four sources as the proper motion cluster membership probability, and average that with the RV membership probability for each star to get our final value. Two stars don't have any proper motion probabilities from literature; for these we assign the RV membership probability.

E.8. *NGC 2548*

Barnes et al. (2015) use photometry to determine cluster membership probabilities. They also provide the cluster member classification from Balaguer-Núñez et al. (2005), however not every star has a crossmatch in that catalog. Therefore we use the classification of "provisional members" and "confirmed members", to which we assign membership probabilities of 0.7 and 0.9 respectively.

E.9. *M34*

In the Meibom et al. (2011) M34 catalog, stars are either classified as kinematic (and photometric) members, or just photometric members. For the kinematic members, a radial velocity membership probability is provided, and in some cases a photometric probability is too. We take the average of these where both are available, and take the radial velocity value  $P_{mem,RV}$  where not. We assign a membership probability of 0.7 to the only-photometric members.

E.10. *H Persei*

Morax et al. (2013) compiles membership data from Currie et al. (2010), who analyze both spectroscopic and photometric membership. Currie et al. (2010) estimate a 16% contamination rate in their photometric catalog, so we assign a value of 0.84 cluster membership probability for their (only) photometric members. We also assign a membership probability of 0.84 for spectroscopic only members, and 0.9 for stars that are both photometric and spectroscopic members. For stars in the Morax et al. (2013) catalog that they do not report a membership category from Currie et al. (2010) from, we assign a value of 0.7, as no quantitative membership probabilities are provided by Morax et al. (2013). For non-members according to Currie et al. (2010), we assign a value of 0.5.

E.11. *Curtis et al. (2019): NGC 6811*

For NGC 6811, Curtis et al. (2019) apply astrometric cuts, followed by photometric cuts applied on a Gaia G vs. BP-RP CMD. They do not provide individual cluster membership probabilities, so we assign a value of 0.9 to all stars.

E.12. *Curtis et al. (2020): NGC 752, NGC 6819, Pleiades, Ruprecht 147*

For the Pleiades, NGC 752, and NGC 6819, Curtis et al. (2020) applied Gaia DR2 astrometry, RVs and CMDs to identify single star members in the same method as for Ruprecht 147. For Ruprecht 147, they used proper motion candidates from literature, filtered that list using radial velocities, and merged further Gaia DR2-based catalogs from literature. We assign a cluster membership probability of 0.9 to all of these candidates.

### E.13. *Upper Scorpius and $\rho$ Ophiucus subgroups*

As part of their census of the Sco-Cen region, [Ratzenböck et al. \(2023\)](#) provide “stability values” for the membership of each Gaia DR3 star in their corresponding groups. We use this as our cluster membership probability.

### E.14. *Taurus*

[Krolikowski et al. \(2021\)](#) do not provide cluster membership probabilities for the Taurus sub-groups, so we adopt a value of 0.9. For most of these groups, the ages are very similar so the effect of miscategorizing them would be negligible.

## F. MODEL PERFORMANCE TESTS

Here we provide further details on the tests we executed to evaluate the performance of **ChronoFlow**, as described briefly in §5. We used the average stellar log probability as a benchmark metric to measure how well observations align with our  $P_{rot}$  density probabilities (e.g., Figures 7 and 8). Averaging the stellar log probabilities accounts for the different sample sizes of each cluster.

### F.1. *Model performance by cluster*

This test was designed to evaluate how well **ChronoFlow** fits the observational data for each cluster. We calculated the individual stellar log probabilities using the LOOCV models and have plotted these distributions for each cluster in Figure 21. The absolute  $\mathcal{P}_f$  values for each cluster are not particularly meaningful; the probability densities are non-zero across our entire parameter space so we do not expect to achieve anything close to 1. But, the difference in  $\mathcal{P}_f$  between clusters is meaningful. In particular, we note that four of the five clusters highlighted in §5.1 as anomalies (excluding M34) all have a relatively poor fit here as well. The bimodality present in some clusters (e.g., Hyades, NGC 2281, M37, and H Persei) is also meaningful, indicating that there is a better fitting group of stars and a poorer fitting group. In H Persei, this clearly corresponds to the group of slow rotators that fit the model well, and the over-density of fast rotators that is unexpected given its age. In M37 and NGC 2281, the poorer fitting groups seem to be overdensities of intermediate rotators at a wide range of colors lying in the gap between the slow and fast sequences. In Hyades, this appears to be due to intermediate rotators as well, but in this case they are restricted to a  $(BP - RP)_0$  range of  $\approx 2-3$ .

### F.2. *Simulated data tests*

A different test was required to evaluate **ChronoFlow**’s overall performance. To do this, we simulated data from the conditional probability densities that our model learned. If **ChronoFlow** could simulate data that closely approximated observations, we could be confident that it was learning the conditional probabilities well. In this test, we used our predicted probability density distributions from the LOOCV exercise to simulate rotation periods at the observed  $(BP - RP)_0$ ,  $p_{cl}$ ,  $\tau$ , and  $\sigma_{C_0}$  values in our catalog. We drew 200 samples for each observed star, and compared the resulting log probabilities from our simulated data against those from the observations. Figure 22 summarizes these results, averaging the log probabilities per cluster. Our model fits slightly better overall to the sampled data than the observations, however the difference is small relative to the scatter within each cluster. The difference is also cluster dependent; the five anomalous clusters discussed in §5.1 have larger differences on average than the others, but there are some clusters where the fit is actually better to the observations than the simulations. Given the scatter in this difference between clusters and between stars in a cluster, we conclude that **ChronoFlow** can model observed rotational evolution with high accuracy.

### F.3. *Impact of varying photometric uncertainty*

Figure 23 presents the results of varying  $\sigma_{C_0}$  while keeping the other parameters constant for five different ages. As expected, greater photometric uncertainty smooths out the distribution. This is a combination of two factors: (i) there is inherently more scatter in the  $P_{rot} - C_0$  relationship when  $\sigma_{C_0}$  is larger, and (ii) at large values of  $\sigma_{C_0}$  there is less training data (see the pink bars), so the learned density distributions are naturally less constrained in that regime. Therefore, **ChronoFlow** will naturally have more uncertainty in age predictions when  $\sigma_{C_0}$  is larger.

## G. SYSTEMATIC TESTS

Here we provide additional details of the systematic tests and results that were summarized in §6

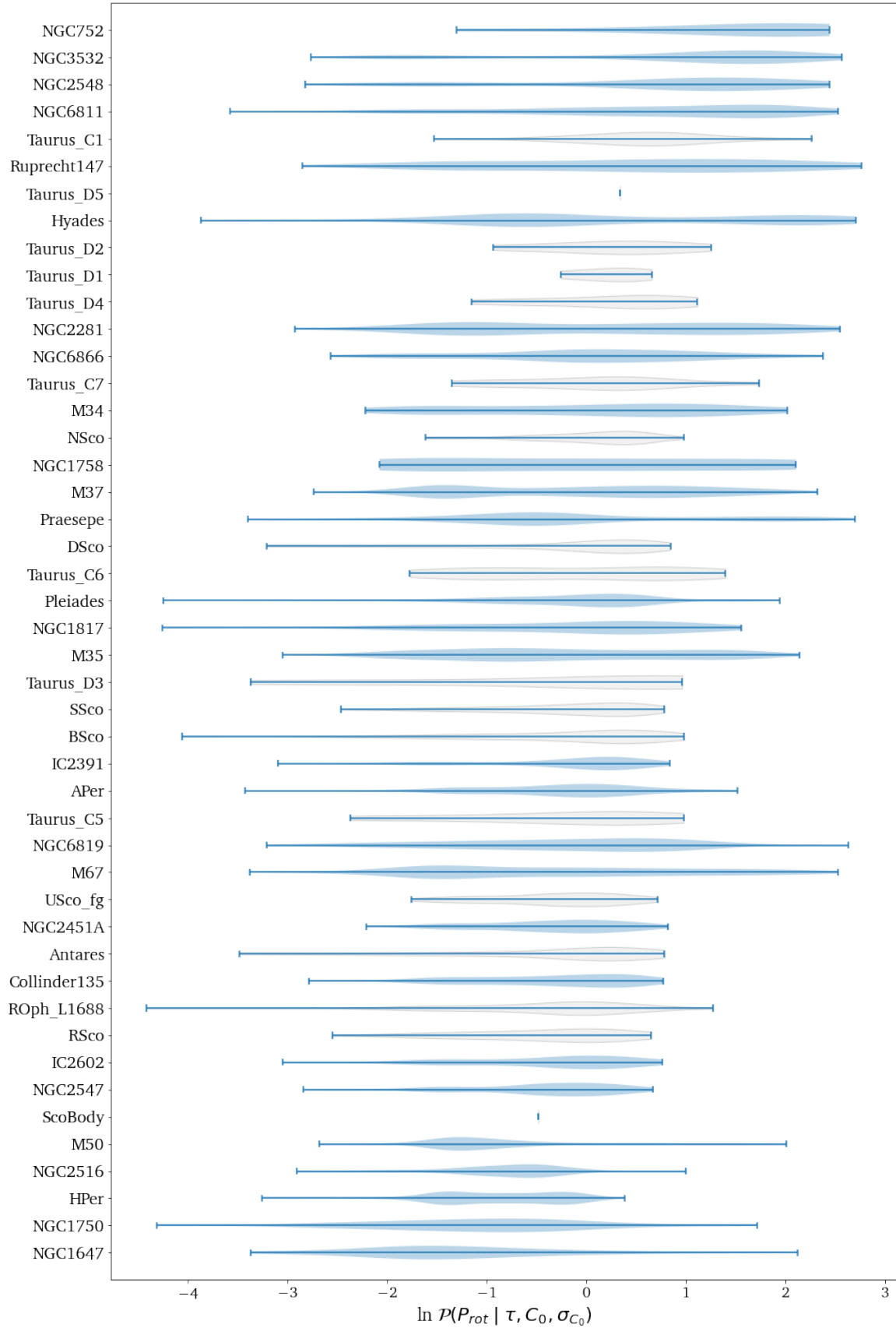


**Figure 21.** Distribution of stellar log probabilities for each cluster. Clusters shaded grey are sub-groups of the Taurus and Sco-Cen regions. Clusters are ordered from best fit and the top to worst fit at the bottom; some exhibit a clear bimodality.

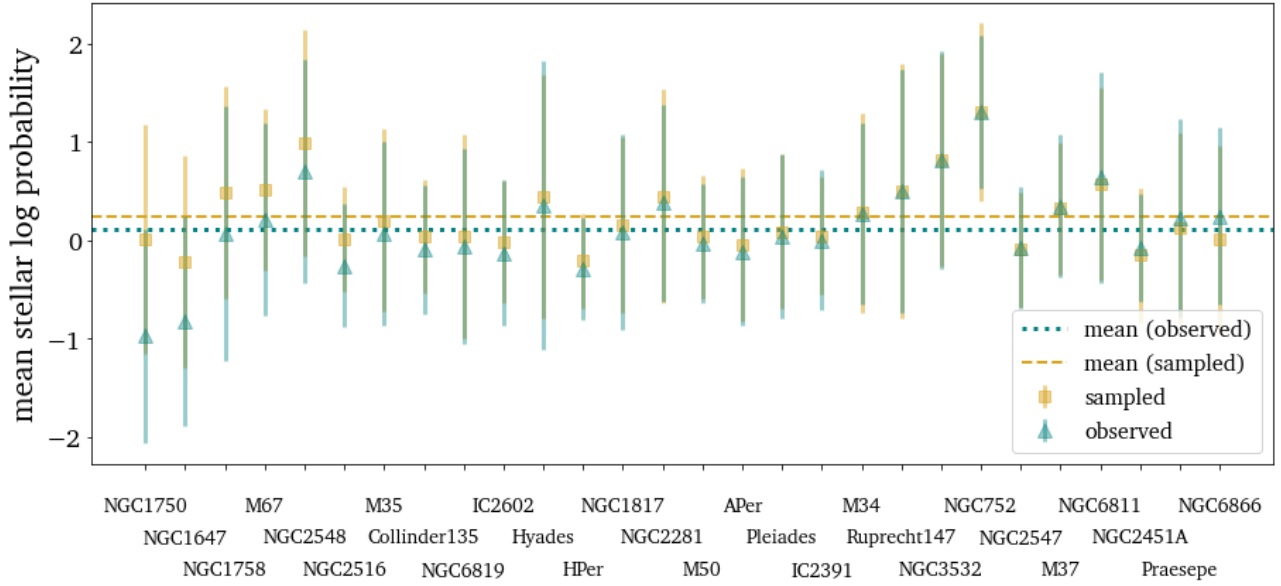


**Figure 22.** Comparison of the stellar log probability distributions for each cluster, calculated using observed data (teal triangles) and 200 samples (per observed star) simulated by ChronoFlow (gold squares). Clusters are ordered by difference between observed and sampled, where those with the poorest fit to observed data relative to sampled data are shown on the left.

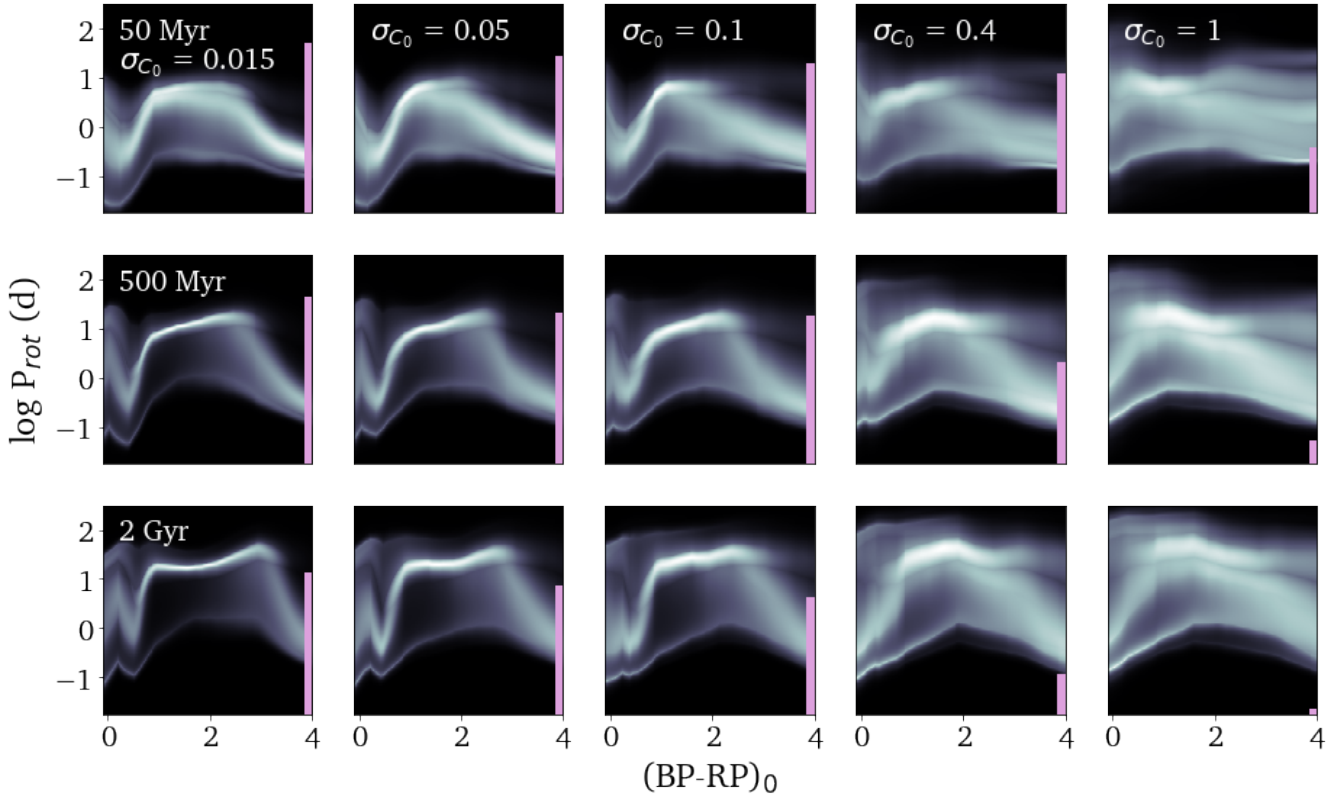


**Figure 23.** The effect of varying  $\sigma_{C_0}$  on model predictions. Probability density slices in  $(BP - RP)_0 - P_{rot}$  space are shown as a function of age and  $\sigma_{C_0}$ . The pink bars indicate the relative number of stars in each bin (scaled exponentially).

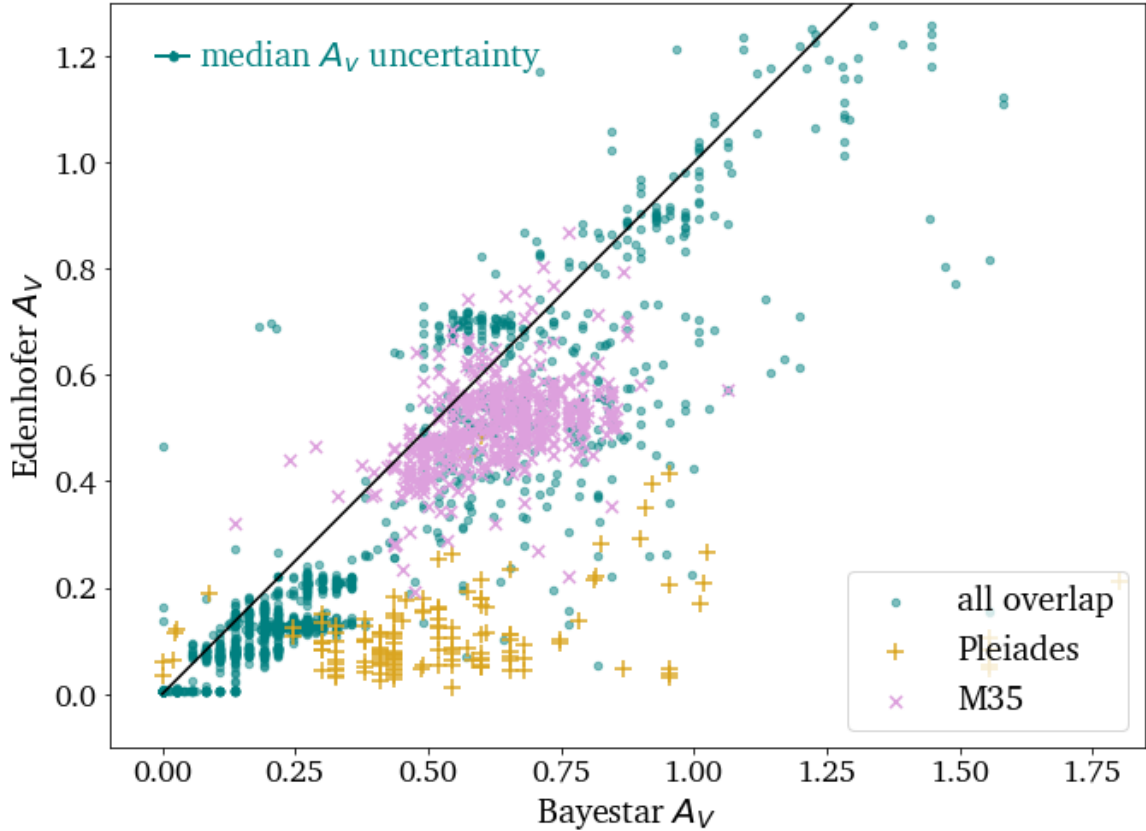


**Figure 24.** Comparison of the extinction on our catalog stars calculated using Edenhofer et al. (2023) and Green et al. (2019). The median uncertainty is shown in both directions in the upper left for reference (note that the Edenhofer uncertainty is much smaller than the Bayestar).

### G.1. Dustmap comparison

There is a systematic due to the choice of dustmap used to calculate extinctions. Extinction uncertainties are non-trivial due to: (i) parallax (and thus distance) uncertainties, (ii) sampling uncertainties within a single dustmap, and (iii) conversion uncertainties for each photometric band. They are the dominant source of photometric uncertainty in our final data catalog (compared to Gaia systematics and DR3 BP and RP uncertainties). In Figure 24 we present a comparison of  $A_V$  calculated from the Edenhofer et al. (2023) (E23) and Green et al. (2019) (B19) dustmaps for stars in our catalog that are covered by both. The  $A_V$  values obtained from the E23 map are systematically lower than those obtained from the B19 map. These results are qualitatively consistent with those found by Diego Godoy-Rivera in a study of Kepler stars covered by both maps (submitted). To analyze the effect on our gyrochronology model, we examined two clusters in detail that have the largest differences, and which each have many stars covered by both maps: the Pleiades and M35. For each cluster, we generated a cluster posterior age probability distribution in four ways, essentially testing each combination of dustmaps for both training and testing:

1. Using LOOCV, we trained a model using the E23 extinctions where there was overlap in coverage, and evaluated the cluster posteriors with E23 photometry.
2. We trained a model using the E23 extinctions, but used B19 to infer the cluster ages.
3. We trained a model using the B19 extinctions, but used E23 to infer the cluster ages.
4. We trained a model using the B19 extinctions, and used B19 photometry to infer the cluster ages.

The resulting posteriors for each test case are shown in figures 25 and 26. The scatter for all four tests for the Pleiades was small ( $\sigma = 0.014$  dex). The M35 age estimates are more scattered, however *the age estimates were consistent*

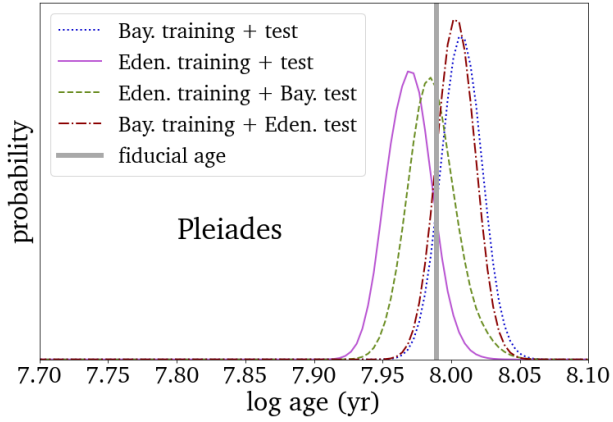


**Figure 25.** Cluster age posterior probabilities for the Pleiades for each of our four test cases comparing the E23 and B19 dustmaps.

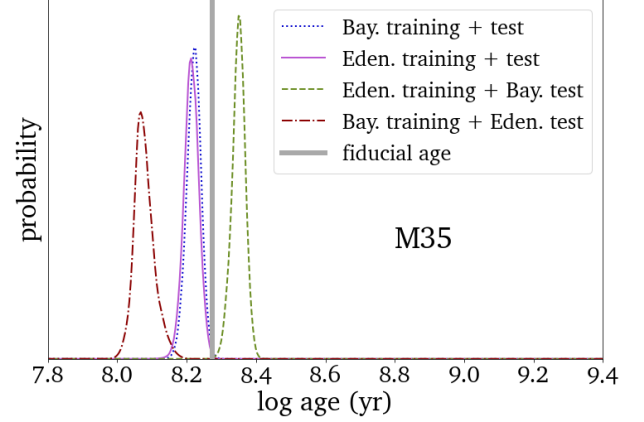


**Figure 26.** Cluster age posterior probabilities for M35 for each of our four test cases comparing the E23 and B19 dustmaps.

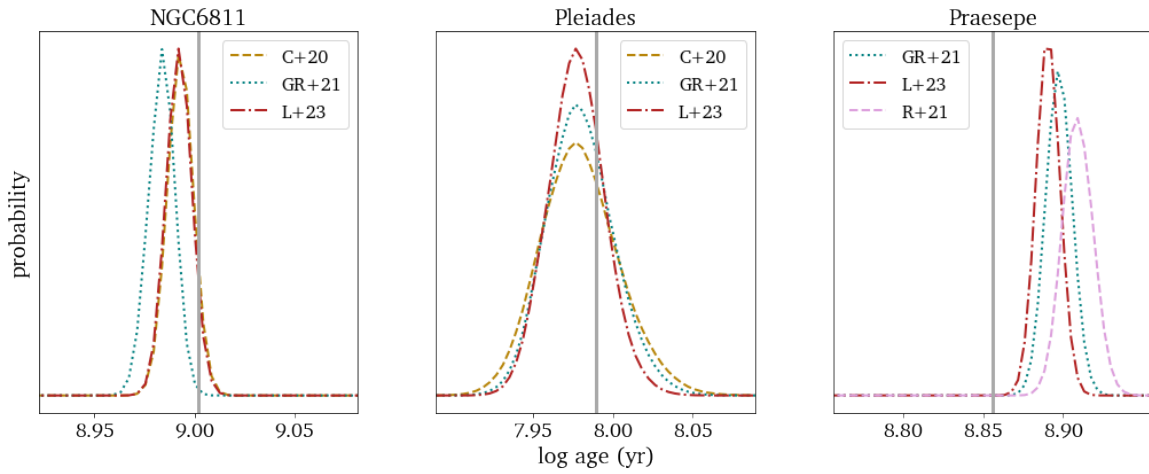


**Figure 27.** A comparison of the LOOCV results for three clusters when the test data were selected exclusively from individual membership catalogs: [Curtis et al. 2020](#) (C+20), [Godoy-Rivera et al. 2021](#) (GR+21), [Long et al. 2023](#) (L+23), and [Rampalli et al. 2021](#) (R+21). The vertical grey line represents the fiducial cluster age. Note that for NGC 6811, the C+20 and L+23 posteriors overlap almost completely. The scatter in inferred ages due to this effect is 0.01 dex.

when the training dust map was the same as the test dust map. Analyzing the results in a different way, we calculated the scatter in age estimates for both clusters to be 0.01 dex when comparing test cases in which a single dustmap was used. The test cases where dustmaps were mixed resulted in an uncertainty of 0.04 dex. These indicate that the systematic uncertainty due to choice of dustmap is small, *if the dustmap is used consistently*. However, caution should be taken when applying ChronoFlow to photometry de-reddened with a method other than the E23 or B19 maps.

### G.2. Source survey (space vs. ground)

We included observations from a variety of both space based and ground based source surveys in our data catalog. Overall, 36% of our data are from ground surveys, and we do not have any space data for M34, M50, NGC 2281, NGC 2516, NGC 2548, NGC 3532, or NGC 752. Given the additional complications associated with observing from ground-based facilities (eg. atmospheric effects, discontinuous data due to the Earth’s rotation), we wanted to determine whether ground data would introduce systematics not seen in only space data. To test this, we executed a LOOCV test using only rotation periods sourced from space surveys. The median cluster absolute residual increased by 3%, and there was no apparent reduction in systematic uncertainties. This indicates that the value of adding more data from ground-based surveys outweighs the reduction in homogeneity of our catalog.

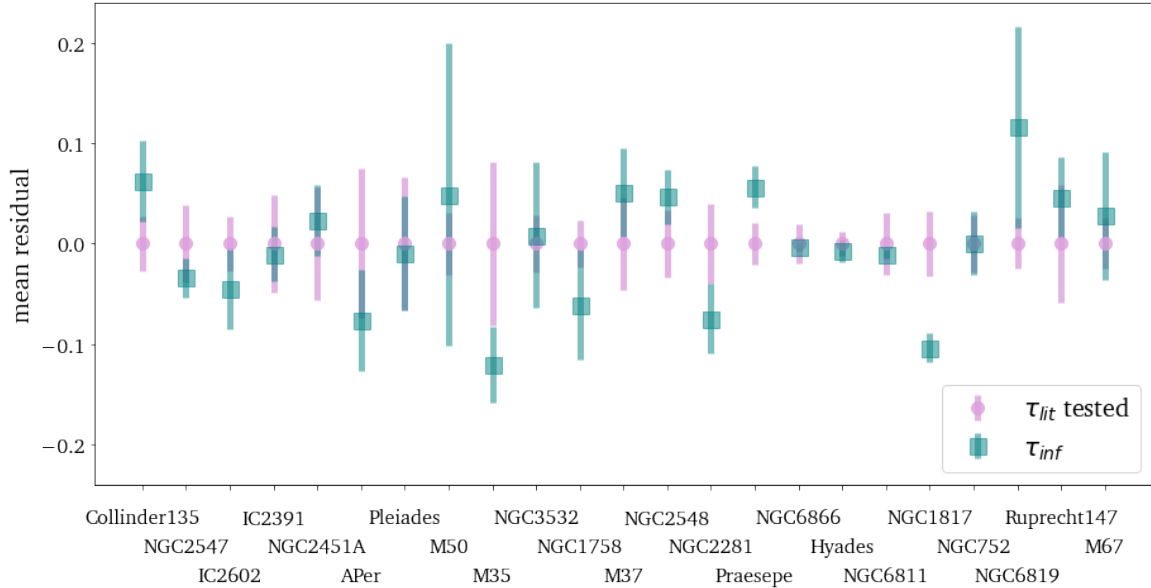


**Figure 28.** A comparison of the mean and variation ( $1\sigma$  shown) in residuals from five different LOOCV models. The pink lines indicate the standard deviation in literature values used for each cluster across the models. The young sub-groups of Taurus and Scorpius are not shown here, nor are the five outlier clusters discussed in §5.1.1.

### G.3. Cluster membership

Using our LOOCV models, we inferred ages using different observational data sets of the same cluster, from different literature cluster membership catalogs. Since we have three distinct literature catalogs for the Pleiades, Praesepe, and NGC 6811, we used these as test clusters.

Results are presented in Figure 27, which shows that there is little variance in the inferred ages ( $\sigma = 0.01$  dex). This suggests that overall, ChronoFlow is robust against cluster membership choices. However, it should be noted that these clusters are well sampled; different cluster membership datasets covering completely different parameter spaces may have more significant variation.

### G.4. Influence of training ages

Since cluster ages are model dependent, it is important to examine the impact that varying calibration ages has. We did this by analyzing LOOCV results using five different version of ChronoFlow:

1. The base model trained on all clusters excluding H Persei.
2. We instead used Lithium depletion ages for the clusters that have such estimates available ( $\alpha$  Persei, IC 2391, IC 2602, NGC 2451A, NGC 2547, and Pleiades). These estimates come from [Stauffer et al. \(1998\)](#), [Stauffer et al. \(1999\)](#), [Oliveira et al. \(2003\)](#), [Jeffries & Oliveira \(2005\)](#), [Gutiérrez Albarrán et al. \(2020\)](#), [Galindo-Guil et al. \(2022\)](#), and [Jeffries et al. \(2023a\)](#). For clusters where multiple estimates were available, we took the geometric average.
3. A model where we have taken the average age from *all* literature sources described in table 2 instead of just the four primary catalogs.
4. Ages directly from [Cantat-Gaudin et al. \(2020\)](#). Since they do not provide ages for Hyades or M34, we instead use the [Bossini et al. \(2019\)](#) age for M34 and the [Gaia Collaboration et al. \(2018\)](#) age for Hyades.
5. A model where we prioritize the B+19 and G+18 ages where available, then L+23, then CG+20. We use the average of B+19 and G+18 for 11 clusters (where both have estimates), just B+19 for eight clusters, G+18 for four clusters, L+23 for two clusters, and CG+20 for the last three clusters.

For the young sub-groups, we used the ages provided by [Ratzenböck et al. \(2023\)](#) and [Krolikowski et al. \(2021\)](#) for all models.

We performed this exercise to emulate the effect of model-dependent uncertainty in training ages (e.g., between lithium depletion, eclipsing binaries, isochrone families, asteroseismology). We compare the resulting variance in age inference relative to the variance in training ages in [Figure 28](#). We also show the mean residual of the inferred age on the plot, but note that is a separated systematic captured by the LOOCV test, and here we are focused on the variance due to calibration ages. As expected, for age ranges where there is more variance in calibration ages, there is more variance in inferred residuals (e.g., at the ages of  $\approx \alpha$  Persei to NGC 3532). M50 and NGC 6819 are the most susceptible to the variation, with scatter exceeding 0.1 dex.

Overall, the age recovery variance is on the same order as the calibration variance. This indicates that varying training ages will have a similar order effect on the inferred ages in the model, which is  $\approx 0.04$  dex.